ABSTRACT

ADIGA, SHASHISHEKAR PARAMPALLI. APPLICATION OF MOLECULAR MODELING TO POLYMER GRAFTED NANOSTRUCTURES.

(Under the direction of Professor Donald W. Brenner)

Polymer chains undergo conformational transitions in response to a change in solvent quality of their environment, making them strong candidates to be used in smart nanometer-scale devices. In the present work molecular modeling is used to explore grafted polymer structures with various functionalities. The first part of this research focuses on two examples of selective transport through nanopores modified with polymer brush structures. The first is the investigation of solvent flow through nanopores grafted with linear chains. Molecular dynamics (MD) simulations are used to demonstrate how a stretch-collapse transition in grafted polymer chains can be used to control solvent flow rate through a nanopore in response to environmental stimuli. A continuum fluid dynamics method based on porous layer model for describing flow through the smart nanopore is described and its accuracy is analyzed by comparing with the results from MD simulations. The continuum method is then applied to determine regulation of water permeation in response to pH through a poly(L-glutamic acid) grafted nanoporous membrane. A second example is use of a rod-coil transition in "bottle brush" molecules that are grafted to the inside of a nanopore to size select macromolecules as they diffuse through the functionalized nanopores. These stimuli-responsive nanopores have a variety

of potential applications including molecular sorting, smart drug delivery, and ultrafiltration, as well as controlled chemical release.

Tethered polymers play an important role in biological structures as well. In the second part of the research, application of atomistic simulations to characterize the effect of phosphorylation on neurofilament structure is presented. Neurofilaments are intermediate filaments that regulate axonal diameter through their long, flexible side arms extending from the central core. Their functionality is imparted by polymer brush like structure that causes steric repulsion between the filaments. A disruption in their structure/distribution is a hallmark of several neuromuscular diseases including amyotrophic lateral sclerosis (ALS). Further, there is evidence that phosphorylation alters the structure of side arms, which is thought to be associated with ALS. MD simulations are performed to characterize the structure of neurofilament side arms as a function of phosphorylation. The simulations indicate that phosphorylation significantly alters the side arm size, which may affect the axonal caliber. The results may also shed light on the mechanism of ALS.

APPLICATION OF MOLECULAR MODELING TO POLYMER GRAFTED NANOSTRUCTURES

By

SHASHISHEKAR P. ADIGA

A dissertation submitted to the Graduate Faculty of
North Carolina State University in partial
fulfillment of the requirements for the Degree of
Doctor of Philosophy

DEPARTMENT OF MATERIALS SCIENCE AND ENGINEERING

Raleigh, North Carolina
December 19, 2003

Approved By:

Dr. C. Maurice Balik

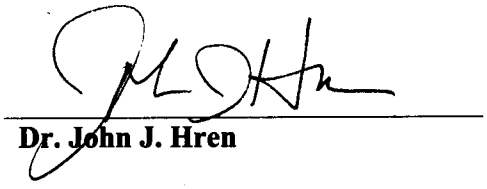

Dr. John J. Hren

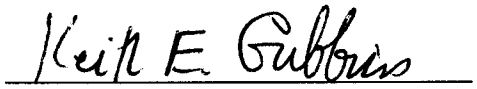

Dr. Keith E. Gubbins

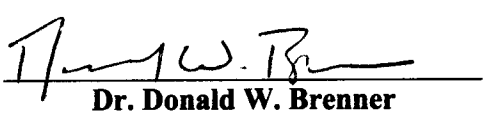

Dr. Donald W. Brenner
Chairman of Advisory Committee

BIOGRAPHICAL SKETCH

Shashishekar P. Adiga was born in Saligrama, a small town on the west coast of India in 1974. He received a Bachelor of Engineering degree in Metallurgical Engineering from Regional Engineering College, Surathkal (now known as National Institute of Technology, Karnataka), India, in 1995. He then enrolled at the Indian Institute of Science, Bangalore, for a Master of Engineering (M.E.) degree in Metallurgy. After completing his M.E. he enrolled for a PhD program in the department of Materials Science and Engineering at North Carolina State University in the Fall of 1997. He plans assume a postdoctoral position in the Materials Science Division of Argonne National Laboratory, Illinois, in February 2004.

ACKNOWLEDGMENTS

I would like to thank my advisor, Dr. Brenner for introducing me to this exciting field of research as well as for his guidance and encouragement during the course of this work. I would like to thank my committee members Dr. Balik, Dr. Hren and Dr. Gubbins for useful discussions during the course of this work. I would like to thank Dr. Jan Genzer, Department of Chemical Engineering for serving as an examiner during my final oral examination.

I would like to acknowledge NASA Ames for supporting this research through a grant. I would like to recognize Dr. Meyya Meyyapan and Dr. Deepak Srivastava of NASA Ames for their interest in this work. I would also like to acknowledge a grant of computing time from the North Carolina Supercomputing Center. I thank Dr. Celeste Sagui, Department of Physics and Dr. Jan Hoh of Johns Hopkins University for helpful discussions. I would like to extend my gratitude to the past and present members of Dr. Brenner's research group, in particular, Dave, Yanxin, Dennis, Olga, Sarah, Kai, and Cliff for their help, suggestions and insightful discussions.

Finally, I would like to thank my parents, sisters, brother and friends for their support and encouragement throughout the course my PhD.

Table of Contents

List of Tables

List of Figures

1 Introduction

Polymers constitute an important class of materials whose production exceeds that of metals even though they have only been known for less than a century [1]. With the emergence of nanoscience/technology as a frontier research field over the past decade, polymers have naturally been considered as candidates to be used in nanometer scale devices. There is an added interest in polymers that arise from their close connection with biology. A biological cell is a brilliant working example of nanotechnology. A majority of their functionality is achieved through a conformational transition of proteins (naturally occurring polymers) in response to environmental stimuli [2]. As biological nanosystems have been envisioned to provide excellent models as well as applications for the development of nanotechnology, polymers, which are also capable of environment-responsive conformational transitions, become an obvious choice for mimicking the structure/function of biomacromolecules. Historically, the advancement of polymer science has complemented the development of molecular biology [3,4,5]. The development of polymer physics has helped the understanding of complex biomolecular mechanisms. It is in this sense that polymer science, biology and nanotechnology are closely related. As we will discover in this Dissertation, just as biological systems inspire smart nanodevices, the well-established concepts of polymer physics can be useful in understanding bionanostructures.

The work presented in this Dissertation is concerned primarily with molecular modeling of polymer grafted nanoporous structures. Nanoporous materials constitute a class of structures containing pores with sizes ranging from tenths to tens of nanometers. Common examples include zeolites, activated carbons, some metal oxides, silicates, and other porous glasses. Nanoporous materials are used in a number of applications, including fluid separation, ultrafiltration, and as catalysts and catalyst supports. They may also find use for energy storage, for inducing novel reactions, and for device fabrication over molecular dimensions. Nanoporous systems based on biological structures such as DNA-membrane complexes have also been proposed [6]. While the more traditional nanoporous materials base their transport selectivity on features such as charge [7] and molecular size there has been a great interest in building additional functionality into nanopores in the last few years. For example, smart nanoporous structures that can open/close in response to environmental stimuli, i.e. pore sizes that can dynamically respond to the nature of surrounding solvent, have been explored. This novel structure is not without precedence. In biology cell membranes are able to permit the selective transport of molecules in and out of the cells. These membranes include channels that are lined with chain molecules that can change their conformations and thereby cause the pores to open or close in response to changes in pH or ion concentration. Recently, in an attempt to mimic this gating behavior, a variety of synthetic nanoporous membranes have been studied in which liquid or solute permeation was regulated by means of conformational transitions of grafted polymers in response to pH [8], ion concentration [9], and temperature [10]. These unique materials could potentially be used in a wide

variety of applications including smart drug delivery, bio-implants and molecular machines.

To develop these smart nanoporous materials it is critical to understand their properties in a fundamental way. As there have been very few theoretical treatments to study their properties, there is a need for developing a detailed theoretical framework for designing these materials. The goal of this work is to undertake a fundamental understanding of flow regulation and to develop molecular design criteria for this emerging class of nanoporous materials using atomistic simulations and polymer statistical mechanics. In particular, we demonstrate how a combination of modeling techniques that include molecular dynamics simulations, polymer mean-field theory, the theory of conformational transitions of polymers, and continuum fluid mechanics can be used to design polymer grafted nanoporous materials with target properties for specific applications.

The presentation begins in Chapter 2 with a discussion of theories that describe the universal behavior of polymers at interfaces and in solution. In Chapter 3 results from molecular dynamics simulations that are carried out to characterize solvent flow through a polymer grafted cylindrical nanopore in good and poor solvents are presented. The ability of the nanopore to regulate flow based on whether the grafted chains have an extended or a collapsed conformation in a given solvent is demonstrated. By comparing the results of molecular dynamics simulations to numerical solutions of the Brinkman equation we show that continuum fluid mechanics can provide an accurate description of

fluid flow in polymer-grafted nanopores for good and poor solvents provided that an appropriate permeability expression based on polymer layer structure and dynamics is used. This result establishes a critical starting point in nanofluidics from which modeling can be used to design this emerging class of smart nanoporous materials with tailor-made properties.

In Chapter 4, the continuum method based on the Brinkman equation, described in the Chapter 3, is applied to analyze water permeation control through a nanoporous membrane grafted with poly-L-glutamic acid chains. Park and coworkers [8] have demonstrated that a helix-coil transition in poly-L-glutamic acid chains in response to pH change can be used to regulate water permeation through these membranes. We have analyzed the helix-coil transition according to the Zimm-Bragg model to determine the thickness of the grafted polypeptide layer inside a cylindrical nanopore as a function of pH. We then calculated the flow rate through the nanopore as a function of pH. The results are compared with experiments by Park and coworkers. The results establish that polymer statistical mechanical models combined with a continuum porous layer treatment of flow through the polypeptide grafted nanopore can be used to successfully to design smart flow control systems.

In Chapter 5 molecular dynamics simulations have been used to explore a comb polymer grafted ‘smart’ nanoporous system. The dynamic pore sizing capability in these systems is produced by a rod-globule transition in comb polymer molecules that are anchored to the inside of a nanometer-scale pore. The ability of the system to size sort chain

molecules is explored. The simulations indicate that changing the solvent quality can produce a significant change in pore opening which in turn can be used to selectively trap large molecules while allowing smaller molecules to diffuse freely through the pore.

In the final part (Chapter 6) of the Dissertation, the application of molecular modeling to study a neurofilament, a polymer-grafted bio-nanostructure, is presented. Neurofilaments are intermediate filaments that regulate axonal diameter through their long flexible side arms extending from the central core [11]. Besides providing mechanical stability the side chains form a nanoporous network inside an axon that allows nutrients and ions to diffuse. Recent experiments have provided strong evidence for polymer brush like structure of these filaments that impart their functionality [12]. We have performed molecular dynamics simulations to characterize the structure of neurofilament side arms as a function of the degree of phosphorylation.

References

[1] P. G. de Gennes, Introduction to Polymer Dynamics, Cambridge University Press, Cambridge, (1990).

[2] R. A. Freitas, Nanomedicine, Vol. I, Landes Bioscience, (1999).

[3] A. Y. Grosberg, A. R. Khokhlov, Statistical Physics of Macromolecules, AIP Press: New York, (1994).

[4] P. F. Flory, Statistical Mechanics of Chain Molecules, Hanser Publications: New York, (1969).

[5] T. M. Birshtein, and O. B. Ptitsyn, Conformations of Macromolecules, Interscience Publishers, New York, (1966).

[6] G.C.L. Wong, Y. Li, I. Koltover, and C.R. Safinya, App. Phys. Lett. **73**, 2042 (1998).

[7] M. Nishizawa, V. P. Menon, and C. R. Martin, Science, 268, 700 (1995).

[8] Y. S. Park, I. Toshihiro, and Y. Imanishi, Langmuir **16,** 5376 (2000).

[9] Y. Osada, K. Honda, and M. Ohta, J. Memb. Sci. **27**, 327, (1986).

[10] S. Akerman *et al.* Int. J. Pharma. **164**, 29 (1998).

[11] See for example `Neurofilaments', C.A. Marotta, Ed. (University of Minnesota Press, Minneapolis, 1983)

[12] H.G. Brown and J.H. Hoh, Biochemistry, **36**, 15035 (1997).

2 Background on Polymer Physics

2.1 Introduction

Presented in this chapter is an overview of key concepts in polymer physics that are relevant to the problems discussed in subsequent chapters. This overview is not meant to be an exhaustive review of the subject, but rather a starting point from which modeling can be developed to address the specific systems we are considering. Polymers are long chain molecules that consist of monomers (repeating groups of atoms) that are covalently bonded. Depending on whether the constituent monomers are of the same type or different types they are called homopolymers or copolymers, respectively. Polymers are commonly used in many applications, including plastics, paints, coatings, and electronic materials to name a few. Polymers are also being tested for several novel applications; e.g., polymer gels are proposed for controlled drug delivery devices, actuators and sensors [1]. Polymer coated surfaces (polymer brushes) are extensively studied for friction and rheological properties as they promise a new class of low friction surfaces to be used in miniature devices and biological implants [2]. The key for development of such novel devices resides in our ability to control the response of polymer-based systems to changes in their environment. This involves understanding the structure and dynamics of polymer molecules at a microscopic level.

Polymer molecules in solution can be viewed as some sort of random coils that continuously change their shape and size, and the characteristic properties of the system fluctuate around their statistical mean values. Understanding the spatial configurations of

long chain molecules is critical to comprehend the properties of synthetic polymers. The precise nature of conformations of polymer chains is determined by the space available (entropic contribution) and the nature of the constituent monomers and their interaction with the solvent (interaction energy). Typically polymers exhibit a certain universality in their properties that allows for the application of statistical mechanics to study them, hiding the specific molecular details behind simpler concepts such as virial coefficients and flexibility of the chain.

In the beginning of the chapter a presentation of the properties and conformations of neutral polymer chains, polymer chains in solutions, polyelectrolyte chains and polymer brushes is given. A majority of the concepts developed for synthetic polymers are also applicable to biopolymers, although special importance is to be given to specific details. These issues are discussed with regard to protein molecules. Finally, the modeling approach employed in this work is presented.

2.2 **Configurations of Single Polymer Chains**

2.2.1 Ideal Polymer Chains:

The simplest mathematical representation of a polymer chain is based on the random walk model [3]. This model considers a polymer chain of N links, each of length a, that are able to point in any orientation independent of each other. Taking the analogy of the average root mean square displacement after N hops of length a of a particle in Brownian

motion, the average end-to-end distance R of this "freely-jointed" polymer chain can be expressed as

$$\langle R \rangle = aN^{1/2}. \qquad 2.1$$

The random walk model estimates the average distance between the first and the last monomers of a freely jointed, ideal (no interaction between monomers) polymer chain to be proportional to the square root of the number of links. Another important quantity that characterizes the size of a polymer chain is the probability distribution function $P_N(R)$ that gives the probability that the end-to-end distance of the chain of N links is equal to R. For a freely jointed chain this distribution is Gaussian and is given by [4],

$$P_N(R) = \left(\frac{2\pi Na^2}{3}\right)^{-3/2} \exp\left(\frac{-3R^2}{2Na^2}\right). \qquad 2.2$$

This probability distribution has two important implications. First, a Gaussian chain is a very "loose" system with very low concentration ($c=N/R^3 \sim N^{-1/2}\, a^{-3}$) and high fluctuations. The fluctuations are of the order of the average coil size itself. Second, the origin of polymer elasticity can be explained on the basis of this distribution. For a given end-to-end distance R the number of ways the chain links can be arranged is proportional to $P_N(R)$ [4]. The entropic term, which is the only contribution to the free energy of an ideal chain, is

$$U_{el} = TS = -k_B T \log P_N(R) = \frac{3R^2}{2Na^2} + \frac{3}{2}\log\left(\frac{2\pi Na^2}{3}\right). \qquad 2.3$$

In other words, it costs entropy to stretch a chain away from its equilibrium size and the force required to stretch a polymer chain can be estimated as $\mathrm{d}U(R)/\mathrm{d}R = 3\, k_B T\, R/Na^2$.

Thus a polymer chain is a Hookian spring with stiffness that increases with temperature and decreases with the number of links. This simple model is capable of explaining rubber elasticity that has an entropic origin.

There exist ideal chain models with flexibility mechanisms other than free joints, with neighboring links having orientations that are not independent. Typically the orientational correlations diminish very quickly with distance. This means that the random walk model is still applicable, only with a link length that corresponds to the length at which the correlations vanish.

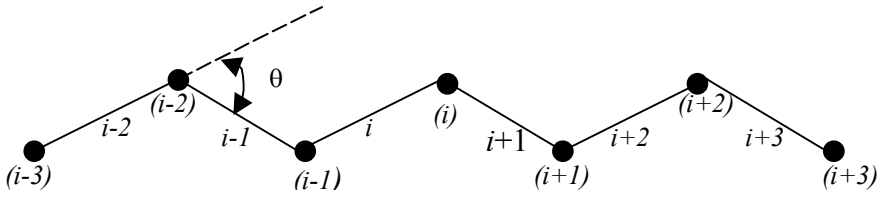

Figure 2.1 Schematic representation of backbone atoms of a chain. Link i leads from atom i-1 to atom i.

For example, if we consider an ideal chain model illustrated in Figure 2.1, that has stiff links of length a, a fixed valence angle θ between neighboring links and a free rotation (i.e. link i is able to point in any direction with respect to the plane formed by links i–1 and i–2), the average mean square end-to-end distance is given by [4],

$$\left\langle R^2 \right\rangle = Na^2 \frac{1+\cos\theta}{1-\cos\theta}. \qquad 2.4$$

If this chain can be thought of as a freely jointed chain with an "effective" segment length l, there are Na/l such segments and the average mean square end-to-end distance is given by,

$$\left\langle R^2 \right\rangle = \left(\frac{Na}{l} \right) l^2 = Nal \,. \qquad 2.5$$

This effective segment length is termed Kuhn's statistical segment length and, by comparing with Eq. 2.2, is $l=a(1+\cos\theta)/(1-\cos\theta)$. Therefore a fixed valence angle with a value $< \pi/2$ has an effect of increasing the chain size, and the smaller the angle the larger the effect. Similar expressions can be derived for the Kuhn length for chains that have fixed rotation angles.

In addition to the Kuhn length there is another characteristic length that is often used to describe chain flexibility, the *persistence length* l_p. This is based on the worm-like chain (WLC) model that considers the chain to be a continuous backbone with a correlation between chain sections that decays exponentially with distance separating them. That is, if we define $\langle \cos\theta(s) \rangle$ as the mean cosine of the angle between the chain segments separated by the length s, the following relationship holds [4],

$$\left\langle \cos\theta(s) \right\rangle = \exp\left(-\frac{s}{l_p} \right). \qquad 2.6$$

The constant l_p is the length above which the segment orientations are uncorrelated and it is of the same magnitude as the Kuhn's length. In fact, for a chain with fixed valence

angle and free internal rotation, the persistence length and Kuhn's length are related as $l=2l_p$.

2.2.2 Polymer chains with volume interactions:

The ideal chain models considered in the previous section included interactions between only the neighboring segments via bonds, valence and dihedral angles. Nevertheless, they are able to capture some important features of long chain molecules including their fluctuations and elasticity. What about the occasional contacts between segments that are far away along the backbone due to thermal fluctuations? These interactions can be steric, Van der Waal's or electrostatic in nature. If we considered steric interactions, which arise from the fact that polymer segments have a finite volume and exclude other segments from occupying this volume, they tend to expand polymer chains from their ideal chain configurations. For this reason steric effects are also termed excluded volume effects. The excluded volume interaction is also termed the long range interaction as opposed to the short range interaction that represents interactions between neighboring segments. It may be pointed out that long and short range is with reference to how far away are the segments along the backbone and not the spatial separation.

To explain the effect of volume interactions on the properties of polymer chains it would be helpful to consider the total interaction energy between all the monomers. The interaction energy can be expressed as a virial expansion given by [5],

$$\frac{U_{\text{int}}}{k_B T} = \int \left[\frac{1}{2} \upsilon c(r)^2 + \frac{1}{6} \omega c(r)^3 + ... \right] dr \,, \qquad 2.7$$

where υ and ω are the second and third virial coefficients, respectively, $c(r)$ is the local monomer concentration, k_B is Boltzmann constant and T is the temperature. For low monomer concentrations the energy can be approximated by the first term neglecting the higher order terms. The second virial coefficient υ is also termed the excluded volume parameter and is related to the interaction energy $U(r)$ between two monomers separated by a distance r as,

$$\upsilon = \int 2\pi r^2 \left[1 - \exp\left(-\frac{U(r)}{k_B T}\right)\right] dr , \qquad 2.8$$

Typically the interaction between monomers has both attractive and repulsive contributions. Figure 2.2 is a schematic plot of the interaction energy between two monomers as a function of distance between them.

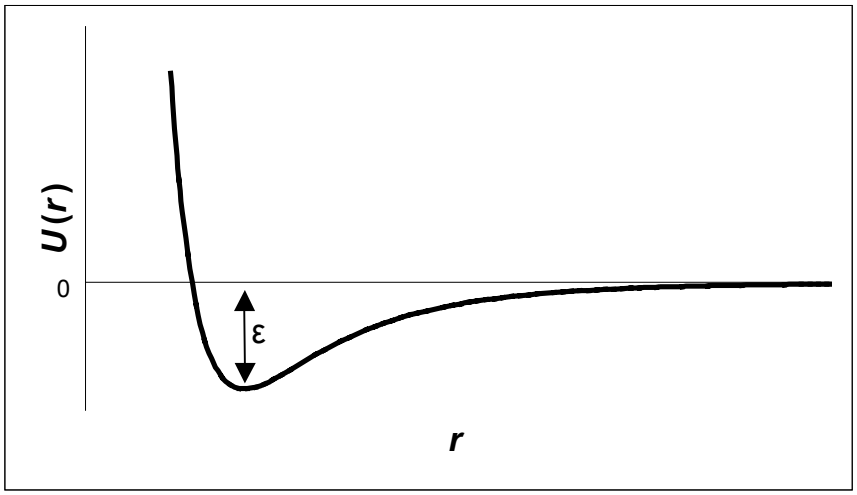

Figure 2.2 A schematic of an interaction potential between non-bonded monomers characterized by a well-depth ε.

The parameter υ is dependent on temperature. For $k_B T >> \varepsilon$ the repulsive interactions are important and υ is positive. Let us consider Flory's method to describe the influence of

excluded volume interactions on chain size. The total free energy of a chain with a volume interaction consists of the elastic energy given by Eq. (2.2) and an interaction energy that can be estimated as follows. The polymer chain can be considered as a monomeric gas confined in a spherical volume of radius R of concentration $c \sim N/R^3$. Approximating the interaction energy by the first term of Eq. (2.7), and disregarding the numerical factor and the term that is independent of R, the total energy of the chain as a function of chain radius R can be written as,

$$\frac{U(R)}{k_B T} \cong \frac{R^2}{Na^2} + \upsilon \frac{N^2}{R^3}. \qquad 2.9$$

The equilibrium value of R is a balance between the excluded volume interaction, which tends to expand the chain, and the entropic term that opposes it. Minimizing $U(R)$ with respect to R gives the equilibrium size of the chain, which is also called the Flory radius. Thus the size of a polymer chain for $\upsilon>0$ scales with the number of monomers as,

$$R \sim N^{3/5} \quad , \qquad 2.10$$

as compared to the square root dependence (Eq. (2.1)) in the case of ideal chains.

For $k_B T << \varepsilon$ attraction between monomers dominates over repulsion and υ is negative. The result is a collapsed chain that has a globular structure with size [4],

$$R \sim N^{1/3}. \qquad 2.11$$

In between expanded and collapsed states, there exists a temperature at which attractions and repulsions compensate each other. This temperature is called the theta point (T_θ) or Flory temperature. At T_θ, the excluded volume parameter $\upsilon=0$, and the chain behaves like an ideal chain with scaling behavior given by Eq. (2.1). In going from a temperature at

which $v>0$ to a temperature at which $v<0$, the polymer chain undergoes a stretch-collapse transition.

In addition to temperature, solvent molecules also can affect the size of polymer chains by modifying the effective interaction $U(r)$ between monomers (solvent mediated interaction). For a given solvent and temperature, if $v>0$, the interaction between monomer and solvent is favored over monomer-monomer interactions that result in an expanded chain, and the solvent is said to be a "good" solvent. If $v<0$, more favorable monomer-monomer interactions cause collapse of the chain, and the solvent is said to be a "poor" solvent. For a solvent in which the monomer-monomer and monomer-solvent interactions are equally favored, $v=0$, and this solvent in which the chain has ideal behavior is called the "theta" solvent. In general, the radius of a polymer chain scales with the number of monomers in the chain as:

$$R \sim N^{\delta}, \qquad 2.12$$

where the exponent δ is equal to 3/5, ½ and 1/3 for good, theta and poor solvents, respectively.

The excluded volume theory just presented breaks down at high chain concentrations, while Flory-Huggins mean field theory becomes valid [6]. In this theory, the polymer chain is modeled as a random walk on a lattice, with each site being occupied either by a monomer or by a solvent molecule. The fraction of sites occupied by monomers Φ is related to the concentration by $\Phi=ca^3$. The free energy for this model has two contributions. The first is the entropy term related to the number of ways the chain can be

arranged on the lattice for a given Φ. The second is the interaction energy between monomers. The total energy of the system is given by,

$$\frac{U}{k_B T} = \frac{\phi}{N}\ln\phi + (1-\phi)\ln(1-\phi) + \chi\phi(1-\phi), \qquad 2.13$$

where $\chi=\chi_{ms}-1/2(\chi_{mm}+\chi_{ss})$ is the Flory interaction parameter describing the contribution of the interaction energy to the energy of mixing. The quantities χ_{mm}, χ_{ss}, and χ_{ms} correspond to the interaction energy between monomer-monomer, solvent-solvent, and monomer-solvent pairs, respectively. For small concentrations (small Φ) the terms in Eq. (2.13) can be expanded as,

$$\frac{U}{k_B T} = \frac{\phi}{N}\ln\phi + \frac{1}{2}\phi^2(1-2\chi) + \frac{1}{6}\phi^3. \qquad 2.14$$

This is directly related to Eq. (2.7) such that $\upsilon=a^3(1-2\chi)$. Hence, in terms of the Flory parameter good solvents correspond to $\chi<1/2$, poor solvents to $\chi>1/2$, and theta solvents to $\chi=1/2$.

2.3 Polymer Solutions

In the previous section we considered properties of isolated polymer chains, which correspond to dilute polymer solutions in which the concentration of chains is so small that the individual chains do not interact with one another. Isolated polymer chains in a good solvent are swollen, and the scaling exponent δ is 3/5 rather than ½. As the concentration of a polymer solution increases the chains get squeezed together and get entangled. The characteristic concentration that separates the concentration regimes corresponding to detached and overlapped polymer chains is the critical concentration c*.

This critical concentration equals the average link concentration inside an isolated polymer chain

$$c^* \sim N/R^3 . \qquad 2.15$$

It can be easily noted that $c^* \sim N^{-1/2}$ and $\sim N^{-4/5}$ for polymer chains in theta and good solvents, respectively. This implies that for $N >> 1$ the value of c^* is very small, that is chains are strongly overlapped although the monomer concentration is very low. This regime between c^* and the concentration at which the volume fraction of monomers Φ is of the order of unity is referred to as "semidilute" [7]. For values of $\Phi \sim 1$, the solution is in the concentrated regime and is often called a polymer melt. Flory drew a fundamental conclusion regarding the conformation of polymer chains in the overlapping, semidilute and concentrated regimes. According to what is known as the "Flory theorem", the size of polymer chains in a good solvent in semidilute and concentrated regimes scales as $N^{1/2}$, i.e. the chain behaves like a Gaussian coil (coil with no volume interactions). The reason for this can be explained as follows: an isolated chain in a good solvent is swollen to minimize contacts between chain monomers. In the case of a homogeneous polymer solution with overlapping chains, swelling of a chain, even though it causes reduction of the fraction of its own monomers, does not bring about reduction in interaction energy, as it will still interact with monomers of neighboring molecules.

In the case of semidilute polymer solutions there exists a correlation length ξ that corresponds to the mesh size of the network of entangled polymers (refer to Fig. 2.3) [7]. On scales below ξ (which is also the blob size) the chains are self-avoiding walks characterized by the scaling law $\xi \sim a g^{\delta}$, with g being the number of monomers per blob.

On scales above ξ the chains are essentially a random walk. It can be noted that $c=g/\xi^3$, which results in the expression

$$\xi \sim c^{\frac{\delta}{1-3\delta}} . \qquad 2.16$$

Thus, for a good solvent, $\xi \sim c^{-3/4}$, the mesh size decreases rapidly with concentration.

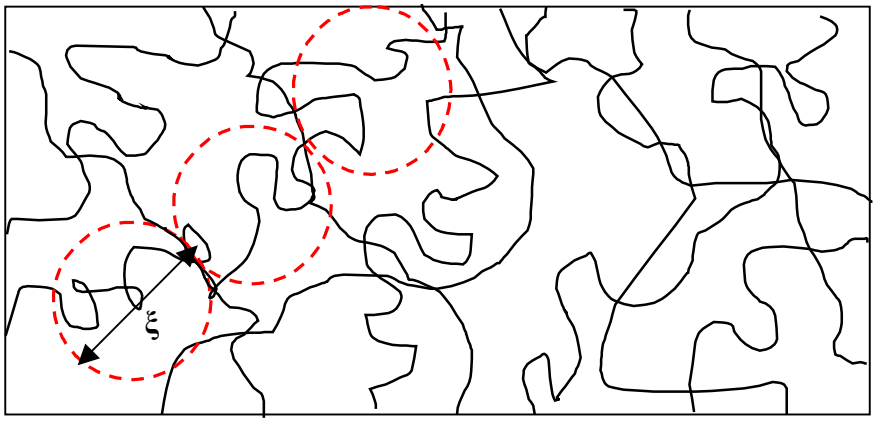

Figure 2.3 The concept of "blob".

2.4 Polyelectrolytes

Polymer chains containing charged links are called polyelectrolytes. Polyelectrolytes are an important class of polymers because many biopolymers including proteins, DNA and RNA are charged macromolecules. Apart from biopolymers there is a significant interest in synthetic polyelectrolytes as well, particularly because they are water soluble. Typically they dissociate in solution to form charged links and low molecular weight counter ions. The presence of counter ions and the possibility of added salt make a polyelectrolyte solution a quaternary system. This, along with the fact that Coulombic interactions between various charges are long range makes polyelectrolyte solution a

rather complex system to study as compared to neutral polymers. Despite these issues there are simple models developed to study the behavior of polyelectrolytes.

Let us consider a polyelectrolyte chain with a fraction *f* of links with a charge *e*. Then, the potential energy of the Coulomb interaction between the charged links *i* and *j* separated by a distance r_{ij} in a solution of dielectric constant ε is [4,8],

$$U(r_{ij}) = (e^2 / \varepsilon r_{ij}) \exp(-r_{ij} / r_D), \qquad 2.17$$

where r_D is the Debye radius determined by the screening of the electrostatic interaction by the ions in the solution. For an ionic strength of the solution *I* this length is given by,

$$r_D = (4\pi I l_B)^{-1/2}. \qquad 2.18$$

Here, $l_B = e^2/4\pi\varepsilon k_B T$, the Bjerrum length, is essentially the distance at which the Coulomb interaction is balanced by thermal energy. We define the Manning parameter, $\lambda = l_B f/a$ (ratio of Bjerrum length and the distance separating charges along the chain backbone, *a*/*f*) that characterizes the strength of the polyelectrolyte chain. For $\lambda << 1$ the Coulombic interaction is dominated by the thermal fluctuations and the chain is weakly affected by electrostatic interactions, hence the term "weak" polyelectrolytes. As the fraction of charged links increases, and for $\lambda \geq 1$ the polyelectrolytes are categorized as "strong". For weak polyelectrolytes, electrostatic interactions at short distances are dominated by thermal energy and the chain still follows scaling laws of neutral polymers. However, at large distances the Coulombic energy can add up and dominate the thermal interactions unless screened by counter ions. Such a chain is a stretched string of blobs for which size R~N, and in the case of a theta solvent the blob size $\xi \approx (a/f^2 l_B)^{1/3} a$.

For strongly charged polyelectrolytes $\xi \sim a$, and the blob theory breaks down and the chain assumes a rod-like configuration. In a solution of sufficiently strong electrolytes, a fraction of counter ions stays in the immediate vicinity of the polymer chains, effectively neutralizing the charge. This phenomenon is referred to as counter ion condensation. The effect of counter ion condensation is to reduce r_D, i.e. to screen Coulombic interactions between links that are distant. This means that on large length scales the chain is essentially a coil. However, on a shorter length scale the electrostatic interactions stiffen the chain, leading to a substantial increase in the persistence length of the chain. The total persistence length of such a chain is the sum of electrostatic persistence length and the persistence length of the uncharged chain.

2.5 Polymer Brushes

Polymer brushes are formed when long chain molecules are attached by one end either to a surface, an interface or to another polymer molecule with a density of attachment high enough so that the chains stretch away from the attachment points much further than the equilibrium size of a free chain [9]. The anchoring mechanism varies with the interface. For solid surfaces the chain end may be chemically attached to the surface or the chain end may adsorb on to the surface. If the interface is between two fluids the fact that the chain end group prefers one medium and the chain prefers the other may be used to form a brush. In the case of polymers grafted to a surface there can be planar, cylindrical and spherical polymer brushes depending on the geometry of the grafting surface. In the limiting case cylindrical and spherical brushes form bottle brush (polymers grafted to a line) and star polymer (polymers grafted to a point), respectively. When several chain

molecules are densily attached to a polymer backbone they form what are called as comb polymers or bottle brush molecules. The spatial constraint of the chains in these structures gives them properties quite different from free polymer chains in solutions. Illustrated in Fig. 2.4 are polymer brush structures in different possible geometries.

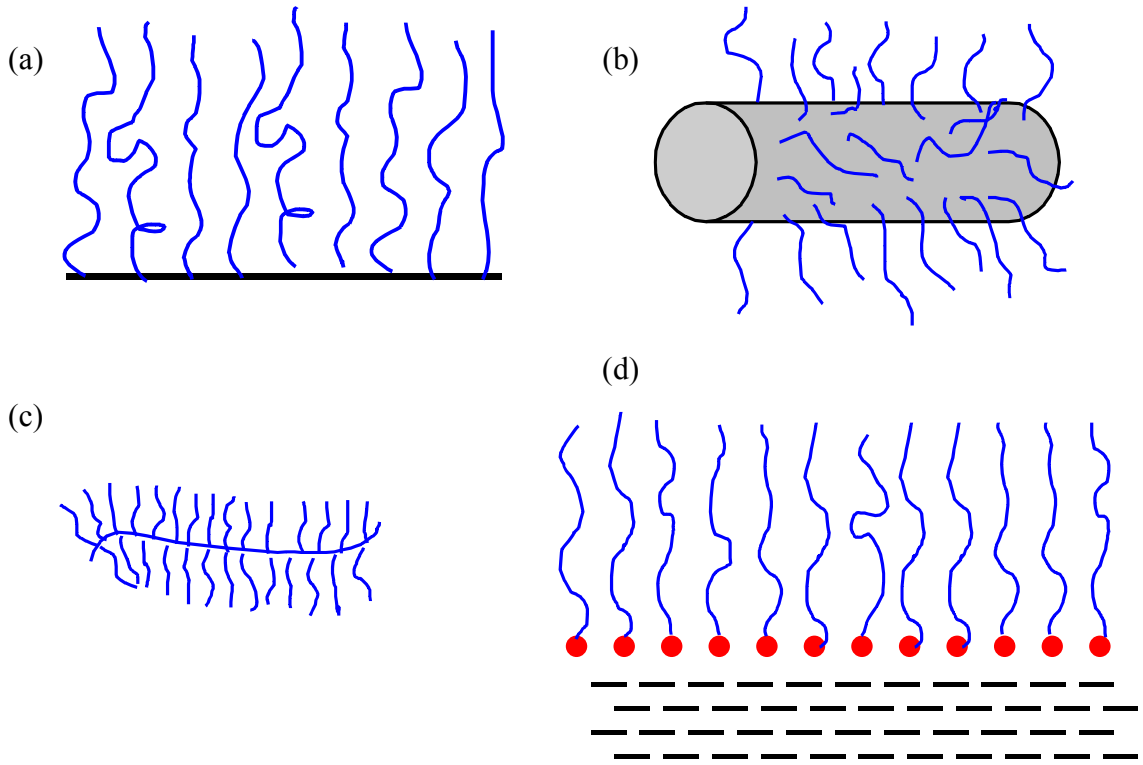

Figure 2.4 Schematic representations of various polymer brushes: (a) Polymers grafted to a planar surface. (b) Polymers grafted to a cylindrical surface. (c) Comb polymer molecule. (d) Polymeric surfactant molecules at the interface of two media.

Polymer brushes form a central model in many important problems in polymer science, colloidal science, lubrication, and biophysics. For example, polymer brushes are used for colloidal stabilization [9]. In this case, solid particles are maintained in suspension by attaching polymer chains; the brushes of two particles resist overlapping, hence avoid flocculaton. The anchoring of the polymer chains close to each other results in molecular

structures that do not overlap with each other due to steric repulsion. Their shape and size are variable and are sensitive to monomer interactions and the environment. The ability to undergo shape and/or size changes in response to the environment (e.g. temperature or pH) or external field (electric field in the case of electrically active polymers) makes them possible candidates as building blocks of nanotechnology. It is interesting to note that several biological structures are also built of such smart biopolymers. For example, neurofilaments [10] (present in axons) and proteoglycan macromolecules [11] (present in cartilage) get their functionality through bottle-brush like structure. Understanding the physical properties of these structures using polymer bottle-brush models may lend new insight into the bio-molecular origins of diseases like amyotrophic lateral sclerosis (a neuromuscular disease thought to be related to neurofilament malfunction) and osteoarthiritis. More importantly, these biomacromolecules could inspire the design of new biomimetic nanostructures to be used in future nanotechnology and nanomedicine.

2.5.1 Polymers grafted to a surface in a good solvent:

Let us consider polymer chains of length N end-attached to a planar surface at a grafting density of one chain per an area s, in a good solvent. If the average distance between the grafting points $d=s^{1/2}$, is very large as compared to the equilibrium size of individual chains then each chain forms a half sphere of radius $R \sim aN^{3/5}$, and does not interact with neighboring chains. However, as distance between the grafting points decreases such that $d<R$, the chains overlap significantly, which results in stretching of the chains away from the grafting surface. As first noted by Alexander [12] and de Gennes [13] the grafted layer assumes a height H such that two energy costs, stretching that reduces

configurational entropy and overlapping that increases the unfavorable interactions between monomers, are balanced. Alexander assumed that the chains are uniformly stretched and the chain ends are located at the outer edge (at *H*) of the brush and that the density of monomers is a constant across the thickness of the brush. The free energy of the grafted layer can then be written in terms of layer height *H* as [14],

$$\frac{U(H)}{k_B T} \cong \frac{H^2}{Na^2} + \upsilon \frac{N^2}{Hs} \qquad 2.19$$

Minimizing this free energy with respect to H, one can find that H scales as

$$H \sim N s^{-1/3} \qquad 2.20$$

That is, the thickness of a densily grafted brush scales linearly with *N* as compared to $R \sim N^{3/5}$ for an isolated chain in a good solvent.

Self-consistent field (SCF) theories [15,16] have also been used to study the properties of grafted polymer layers. These models do not assume that all chains are equally stretched and that the monomer density is uniform across the thickness of the brush. In these models, excluded volume interactions on chain segments at a distance *h* from the surface are incorporated by using a mean-field potential due to all other segments that is proportional to the local monomer concentration *c*(*h*). As the potential field and *c*(*h*) are dependent on one another they are determined self-consistently such that the total energy is minimized. This analysis leads to a parabolic density profile. There are two important implications of a parabolic profile. First, the force required to compress the brush is reduced so that the SCF brush is softer than that of the step function profile brush derived

from scaling analysis. Second, the hydrodynamic penetration depth, which is a measure of how deep a flow past a grafted layer penetrates into the layer, is higher for a SCF brush than a step function brush.

2.5.2 Polymers Grafted to a Surface in a Poor Solvent:

As the quality of the solvent decreases, the structure of brushes changes considerably. The average height of the brush decreases as the solvent quality is reduced. In poor solvents, the monomer density profile is close to that of a step-function profile. There is also an interesting effect below the theta temperature for moderate grafting densities. The polymer brush undergoes lateral phase microsegregation in the form of clusters [17,18]. Several chains aggregate to form a compact core that is connected to the surface through grafted tethers. These structures are referred to as pinned micelles.

2.5.3 Bottle Brush Molecules:

Cylindrical molecular brushes are formed when long chain molecules are densely grafted with relatively long side chains (Figure 2). These can be either copolymer or homopolymer macromolecular structures. For example, polymacromonomers based on polystyrene and poly-(2-vinylpyridine) side chains grafted on a methacrylate backbone are known to form cylindrical brushes [19]. The excluded volume interaction of the side chains cause stretching of the main chain from its equilibrium conformation to adopt a cylindrical brush structure. Depending on the length and density of the side chain and the interaction between them such brushes can attain very high stiffness, with Kuhn statistical segment lengths of the order of 1000 A^o [20].

Depending on the relative stiffness of the main and side chains, one may classify these molecular brushes into four types; (a) rigid backbone – rigid side chains, (b) rigid backbone – flexible side chains, (c) flexible backbone – rigid side chains, and (d) flexible backbone – flexible side chains [21]. We are primarily interested in (b) and (d), which are capable of responding to environmental stimuli.

In a bad solvent a BBM can undergo two types of conformational transitions. In a molecule with a flexible backbone, collapse of the side chains will result in axial contraction of the whole molecule and may result in a globular state as compared to a fully stretched cylindrical brush in a good solvent. For a rigid backbone molecule poor solvent conditions cause microsegregation of the anchored side chains thereby resulting in density modulations along the molecular axis. Recently there have been a number of experimental and theoretical studies on BBMs. Experimental studies mostly involve scanning force microscopy [19,21] and theoretical studies involve Monte Carlo Simulations [22,23].

2.6 Proteins

A majority of biological structures are made up of polymers, specifically proteins, nucleic acids and polysaccharides. These tiny molecular machines play an important role in all biological phenomena from cognition to digestion to locomotion. The biological functions of many of these biomolecules are associated with quite ordinary properties of polymers such as flexibility, volume interactions and entropic elasticity that were

discussed in the preceding sections. For this reason polymer theories form the foundation for understanding the behavior of biomolecules. At the same time biomolecules have certain special features that impart specific functionalities to them. The analysis of these distinguishing features, the reasoning of how one kind of protein is able to detect, for example, a photon of light in the retina of an eye and another type of protein plays an important role in signal transmission through neurons, calls for detailed understanding of the structure of these molecules. Because the problems addressed in this Dissertation are only concerned with proteins, a brief introduction on their structure is presented here.

2.6.1 Structure of Proteins:

Proteins are made up of monomer units that are *residues* of amino acids. Amino acid residues have a general formula –NH-CHR-CO- [24]. There are 20 different amino acids depending on the radical, R. The structure and function of a protein molecule is determined by the number of monomer units (or residues) *N*, and the amino acid sequence. The sequence of amino acid residues is specific to a protein molecule and can be regarded as a kind of "text" written in a 20-character protein alphabet. Table 2.1 lists different amino acids with their letter code and properties.

Table 2.1 Properties and Letter Codes for 20 Amino Acids

Amino acid	3 - letter code	1 - letter code	Properties
Alanine	Ala	A	hydrophobic
Arginine	Arg	R	basic, charged
Asparagine	Asn	N	neutral-polar
Aspartate	Asp	D	acidic, charged
Cysteine	Cys	C	neutral-polar
Glutamine	Gln	Q	neutral-polar
Glycine	Gly	G	hydrophobic
Glutamate	Glu	E	acidic, charged
Histidine	His	H	basic
Isoleucine	Ile	I	hydrophobic
Leucine	Leu	L	hydrophobic
Lysine	Lys	K	basic, charged
Methionine	Met	M	neutral-polar
Phenylalanine	Phe	F	hydrophobic
Proline	Pro	P	conformational, cyclic
Serine	Ser	S	neutral-polar
Threonine	Thr	T	neutral-polar
Tryptophan	Trp	W	Aromatic
Tyrosine	Tyr	Y	Aromatic
Valine	Val	V	Aliphatic, hydrophobic

The spatial structure of three amino acid residues in a protein chain is illustrated in Fig. 2.5. The carbon atom in the –CHR- group is called the α-carbon. The -CO-NH- bond links together –CHR- groups that are specific to each amino acid residue. This bond is called the "peptide" bond. Hence, protein molecules are also referred to as polypeptide chains. A striking characteristic of this linkage between the α-carbon of one unit and the α-carbon of the next unit (the amide group) is that the skeletal bonds are planar [25].

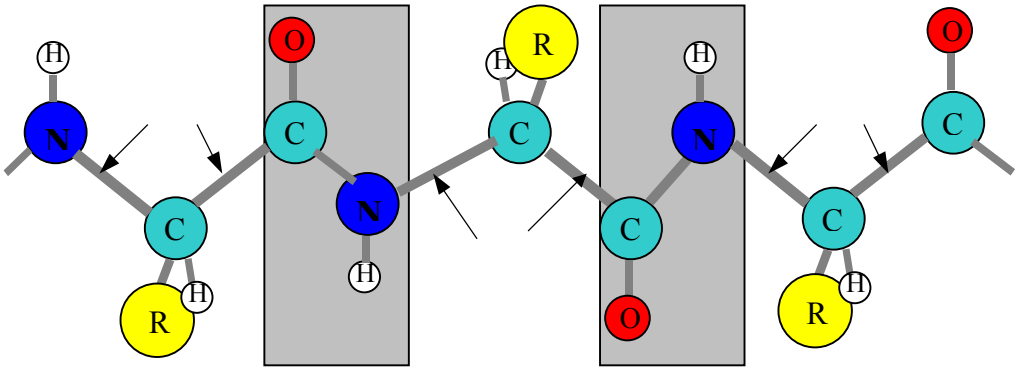

Figure 2.5 The protein chain. The bond between CO of one unit and the NH of the next unit is the peptide bond. The planar amide groups are enclosed in a rectangle. The arrows show the bonds about which the chain may rotate.

This system of bonds and the atoms joined directly by them constitute a *peptide unit*. The amino acid residue is directional because its terminal members NH and CO differ. It does not therefore have an axis of symmetry and this directionality is conferred on the chain as a whole. A polypeptide chain has its two ends terminated by amino and carboxyl groups and these ends are referred to as amino or N-terminal and carboxyl or C-terminal, respectively. All amino acid residues have an asymmetric center –CHR-, except for GLY for which R=H. The asymmetric centers can have two different configurations based on how R and H are placed with respect to the directionality of a residue, namely *L*-residues and *D*-residues. In the polypeptides of living organisms, these centers are predominantly of the *L*-configuration.

The main characteristic of proteins is that they possess a hierarchy of structures viz. primary, secondary and tertiary and sometimes even quaternary structure. The primary structure is the sequence of amino acid residues or the so called “text”, which is formed during the biological synthesis of each molecule. The secondary structure is due to some

sort of short range order in the spatial configuration of chain elements because of the interaction of nearby links in the chain. The main secondary structures of proteins are α-helix or small pins. Finally, the tertiary structure is due to long range or volume interactions as in the case of synthetic polymer chains, which decides, for example, if a protein is a coil or a globule. One of the major challenges in biology today is to determine the secondary and tertiary structure of a protein molecule given the amino acid sequence (i.e. the primary structure). How exactly does a given protein fold into a specific three-dimensional structure? Surely, the problem is of great importance as several diseases are associated with "misfolding" of proteins, either due to mutation in their primary structure or due to environmental conditions. In general, the structure of a polypeptide chain is determined by the permitted C_α-C bond (ψ) and C_α-N bond (φ) angles, the charge (five of the 20 residues are charged under physiological conditions), interaction with the solvent (e.g. hydrophobic or hydrophilic interactions) of each residue in the sequence.

Let us consider for example, the α-helix structure illustrated in Fig. 2.6. Each turn of the helix contains 3.6 amino acid residues, so the period of the helix is 18 residues (5 turns). Each turn corresponds to a displacement of 5.44 A along the helical axis. The α -helix is characterized by angles of internal rotation close to 120^o about the –CO-CHR- and –CHR-NH- bonds of the main chain. The α -helix is stabilized by hydrogen bonds that are formed between C=O of residue *i* and NH of residue *i*+4. The stability of the helical structure is also determined by the amino acid composition. For example the PRO residue is rarely found in helical turns. The amino acid sequence also determines the flexibility of a helical protein. The structure is essentially a one-dimensional crystal. Such an ordered

system can undergo a conformational transition from helix to random coil with changes in temperature, solvent composition or pH of the solution (in the case of polypeptides with charged residues – e.g. GLU). The physical basis of such a transition is the fact that the helix configuration is energetically favorable (due to the formation of hydrogen bonds), while the random coil configuration is favorable entropically [26]. As a result, energies of these two states vary in a different manner with temperature, solvent composition or pH. The transition occurs at a temperature at which these two free energies are identical. The helix-coil transition is co-operative in the sense that the presence of a helical turn in a segment favors the formation of helical turn in the neighboring segment.

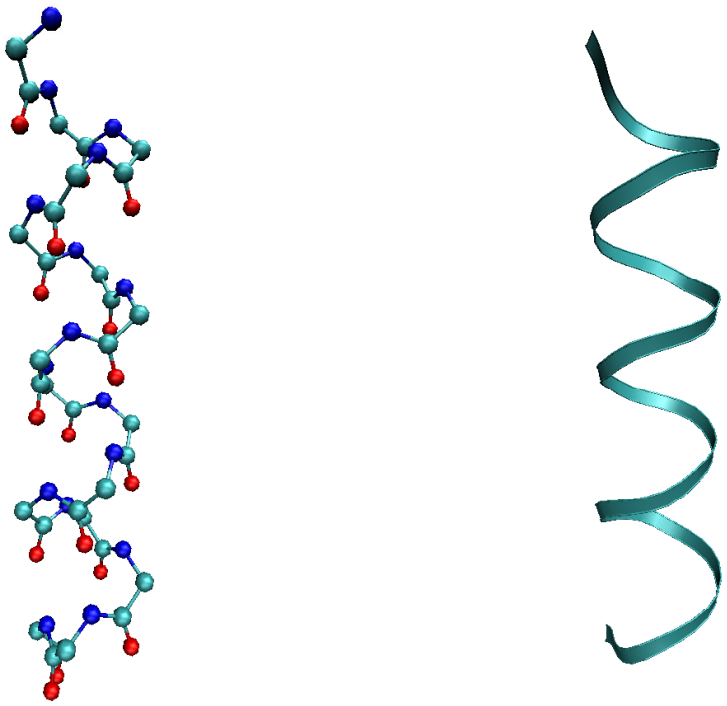

Figure 2.6 The polypeptide α-helix: backbone atoms shown using a ball and stick model (left) and a ribbon illustration (right).

Apart from polypeptides with secondary structures, unstructured polypeptides are also very important among proteins [27]. These are polypeptide chains best described by polymer chain models described in preceding sections. Even though most of the proteins are copolypeptides, they can be treated with utmost simplicity. This is because the skeletal configuration of the copolypeptide chain can be fully represented by a set of virtual bonds connecting neighboring α-carbons, one such bond (of length 3.8 A, same for all residues) being identified with each peptide unit [25]. The internal rotations can be incorporated into polymer models to determine the average dimensions of a chain. It can also be noted that, more often than not, polypeptides are polyelectrolytes. The fraction and type of charges determine the overall conformation of polypeptide chains. Polypeptides can also be polyampholytes, meaning the chain bears residues of both charge types.

2.7 Modeling approach

While theories based on statistical thermodynamics has been helpful in understanding experimentally observed phenomena, they imply several mathematical approximations, the validity of which is hard to judge. On the other hand, computer simulation can study a model of complex polymer structures without any mathematical approximations [28]. Computer simulations provide an important complement to the experimental work and analytical theories. Comparing simulations with experiment helps validate and improve models and could be used to test analytical theories. In view of these advantages, computer simulations have become an established method of research in polymer physics, especially with the advancement in computational power. It must be noted,

though, that molecular simulations of polymers pose particular challenges, considering the large size and long relaxation times encountered.

Several different methods are used to study polymer structures, including molecular dynamics (MD) simulations, Brownian dynamics (BD) simulations, Monte Carlo (MC) simulation as well as self-consistent field (SCF) theory. While the former two methods are designed to capture dynamic properties of polymers, the latter are best suited to study static properties. We have used MD simulations for a majority of the work.

Molecular dynamics (MD) is the premier technique for simulating medium and large-scale molecular systems, including polymers and biological macromolecules. The atoms in a MD simulation system interact through a set of potentials that makes up a forcefield. These potentials are usually parameterized to reproduce experiment or more accurate theory. Summing the potentials as a function of atomic positions produces an overall energy for the system. To illustrate this, let us consider a simple system consisting of a single polymer chain of length N in a pool of solvent molecules. The total energy of the system can be written as,

$$E_{total} = E_{bond} + E_{angle} + E_{torsion} + E_{vdw} + E_{Coulomb} . \qquad 2.21$$

Here, E_{bond} includes the harmonic bond stretch energy between all the bonds,

$$E_{bond} = \sum_{j=1}^{N-1} \frac{k_b}{2}(l_j - l_0)^2 , \qquad 2.22$$

where k_{b} and l_0 are the spring constant and the equilibrium bond length, respectively, specific to each bond. E_{angle} includes the angle bend terms of harmonic type,

$$E_{angle} = \sum_{j=1}^{N-2} \frac{k_\theta}{2}(\theta_j - \theta_0)^2 \ , \qquad 2.23$$

where θ_j is the angle between two adjacent bonds, with k_θ and θ_0 being the force constant and equilibrium value of the bond angle specific to each pair of bond types. The torsion term for a sequence of three bonds j-2, j-1, and j with a dihedral angle Φ_j is defined as,

$$V(\phi_j) = \sum_{n=0}^{12} V_n \cos(n\phi_j) \ , \qquad 2.24$$

such that, the total torsional term is given by,

$$E_{torsion} = \sum_{j=2}^{N-2} V(\phi_j) \, . \qquad 2.25$$

E_{vdw} is the sum of van der Waals interaction between all non-bonded pair of atoms i and j, separated by a distance r_{ij},

$$E_{vdw} = \sum_{i \neq j} U_{LJ}(r_{ij}) \qquad 2.26$$

where $U_{LJ}(r_{ij})$, is typically modeled by the Lennard-Jones potential, that has the form,

$$U_{LJ}(r_{ij}) = 4\varepsilon_{ij}\left\{\left(\frac{\sigma_{ij}}{r_{ij}}\right)^{12} - \left(\frac{\sigma_{ij}}{r_{ij}}\right)^{6}\right\} \qquad 2.27$$

The quantities ε_{ij} and σ_{ij} are energy and distance parameters, respectively, corresponding to a particular pair of particles i and j. E_{colomb} is the energy due to electrostatic interaction between all the charged atoms given by Eq. 2.17.

Given the position of each atom at time t, the forcefield gives the energy E_{total}. The gradient of the energy then provides the force on each atom, which can be used to compute the acceleration, velocity, and positions of each atom at a time $t+\Delta t$ by

numerically integrating classical equations of motion. Thus MD simulations can follow the dynamics of molecules over time. For the sake of brevity the reader is referred to standard books for a detailed description of MD simulations [29]. While MD has the advantage of being able to simulate dynamic properties, the time scale that can be used limits it. Several techniques have been developed to overcome this problem. One of these is using a coarse grained model for the polymer structure.

The work has initially focused on simplified systems using a "bead-spring" model for the polymer chains. Neighboring beads in a chain are connected with a harmonic bond and all non-bonded interactions are modeled using the Lennard-Jones potential. It is well established in the polymer literature that models of this type capture much of the general behavior underlying polymer properties. For simulations of polymer nanostructures using bead-spring models DL_POLY molecular simulation package was used [30].

For biopolymers and polypeptide simulations we have used a detailed forcefield including long range Coulombic interactions. We have used AMBER packages for polypeptide simulations [31]. AMBER (Assisted Model Building with Energy Refinement) refers to two things: a molecular mechanical force field for the simulation of biomolecules (which is in general use in a variety of simulation programs); and a package of molecular simulation programs which includes source code and examples.

References

[1] B. Culshaw, “Smart Structures and Materials”, Artech House Inc Publishers (1995).

[2] G. S. Grest, Phys. Rev. Lett. **76**, 4979 (1996)

[3] A. Y. Grosberg, A. R. Khokhlov, Giant Molecules, Academic Press: San Diego (1997).

[4] A. Y. Grosberg, A. R. Khokhlov, Statistical Physics of Macromolecules, AIP Press: New York (1994).

[5] M. Doi, S. F. Edwards, The Theory of Polymer Dynamics, Clarendon Press: Oxford (1986).

[6] P. F. Flory, Principles of Polymer Chemistry, Cornell University Press: Ithaca, N.Y. (1953).

[7] P. G. de Gennes, Scaling Concepts in Polymer Physics, Cornell University Press: New York (1979).

[8] M. Hara ed. Polyelectrolytes: Science and Technology, Marcel Dekker, Inc. New York (1992).

[9] S. T. Milner, ‘Polymer Brushes’, *Science* **251**, 905 (1991).

[10] See for example `Neurofilaments', C.A. Marotta, Ed., University of Minnesota Press, Minneapolis (1983)

[11] D. Brittan, 'A Window on Arthritis', (WWW reference) URL: http://209.58.177.220/articles/oct96/reporter.html

[14] See for example, R. A. L. Jones, and R. W. Richar, Polymers at Surfaces and Interfaces, Cambridge University Press, Cambridge (1999).

[13] S. Alexander, J. Phys. (Paris) **38**, 977 (1977).

[14] P.-G. de Gennes, *ibid* **37**, 1443, (1976).

[15] S. T. Milner, Macromolecules **24**, 3704, (1991).

[16] Y. B. Zhulina, V. A. Pryamitsyn, O. V. Borisov, Poly. Sci. U.S.S.R., **31**, 205 (1989).

[17] D. R. M. Williams, J. Phys. II, **3**, 1313, (1993).

[18] E. B. Zhulina, T. M. Birshtein, V. A. Pryamitsyn, L. I. Klushin, Macromolecules, **28**, 8612 (1995)

[19] M. Gerle, K. Fischer, S. Roos, A. H. E. Muller,, Manfred Schmidt, S S Sheiko, S. Prokhovora and M. Moller, Macromolecules, **32**, 2629 (1999)

[20] M. Wintermantel, M. Gerle, K. Fischer, M. Schmidt, I. Wataoka, H. Urakawa, K. Kajiwara, and Y. Tsukahara , Macromolecules **29**, 978 (1996).

[21] S. S. Sheiko, M. Moller, Dendimers II, Topics in Current Chemistry **212**, 137 (2001).

[22] Y. Rouault, and O. V. Borisov, **29**, 2605, (1996).

[23] A. Subbotin, M. Saariaho, R. Stepanyan, O. Ikkala, and G. Brinke, Macromolecules **33**, 6168 (2000).

[24] L. Stryer, Biochemistry, Published by W H Freeman & Co., (1999).

[25] P. F. Flory, Statistical Mechanics of Chain Molecules, Hanser Publications: New York (1969).

[26] T. M. Birshtein, and O. B. Ptitsyn, Conformations of Macromolecules, Interscience Publishers, New York (1966).

[27] J. N. Bright, T. B. Woolf, J. H. Hoh, Progress in Biophysics & Molecular Biology, **76**, 131 (2001).

[28] K. Binder, ed. Monte Carlo and Molecular Dynamics Simulations in Polymer Science, Oxford University Press: New York (1995).

[29] See for example, M. P. Allen, D. J. Tildesley, Computer Simulation of Liquids, Clarendon Press: Oxford (1987).

[30] DL_POLY is a package of molecular simulation routine written by W. Smith and T. R. Forester, copyright The Council for the Central Laboratory of the Research Councils, Daresbury Laboratory at Daresbury, Nr. Warrington (1996). For details see http://www.dl.ac.uk/TCSC/Software/DL_POLY/main.html

[31] D.A. Case, D.A. Pearlman, J.W. Caldwell, T.E. Cheatham III, J. Wang, W.S. Ross, C.L. Simmerling, T.A. Darden, K.M. Merz, R.V. Stanton, A.L. Cheng, J.J. Vincent, M. Crowley, V. Tsui, H. Gohlke, R.J. Radmer, Y. Duan, J. Pitera, I. Massova, G.L. Seibel, U.C. Singh, P.K. Weiner and P.A. Kollman (2002), AMBER 7, University of California, San Francisco.

D.A. Pearlman, D.A. Case, J.W. Caldwell, W.S. Ross, T.E. Cheatham, III, S. DeBolt, D. Ferguson, G. Seibel, and P. Kollman. AMBER, a package of computer programs for applying molecular mechanics, normal mode analysis, molecular dynamics and free energy calculations to simulate the structural and energetic properties of molecules. *Comp. Phys. Commun.* **91,** 1 (1995).

3 Modeling of Flow Control Through Polymer Grafted Smart Nanofluidic Channels

3.1 Introduction

Polymer chains bonded to the inside of nanoporous structures are an emerging class of smart nanofluidic "valve" in which responsive gating is achieved through collapse transitions of the tethered polymers in response to changes in fluid conditions. It has been demonstrated, for example, that nanoporous membranes can be made with the ability to regulate fluid flow in response to changes in environmental variables such as pH, temperature, and solvent quality with respect to the grafted polymers [1-4]. In principle, the properties of these smart materials can be tailored to respond to a variety of stimuli, making them ideal for applications that include controlled drug delivery, ultrafiltration, molecular sorting and smart chemical release. Grafting polymers can also reportedly improve fouling resistance of micro- and ultra-filtration membranes [5,6]. A thorough understanding of flow in these systems and the ability to appropriately model this flow is of great significance as they are designed for specific applications.

There has been extensive research, both experimental and theoretical, into understanding the nature of fluid flow in nanofluidic geometries that are not modified with grafted polymers. These studies have demonstrated that continuum fluid mechanics equations are capable of accurately describing Poiseuille flow through channels thicker than about 10-20 atomic diameters [7]. However, molecular simulations have shown that for channels

that are only a few atomic diameters wide, solid walls can induce ordering in liquids, which in turn can produce shear viscosities and microscopic stress tensors during flow that do not match predictions of the Navier-Stokes equations [8,9]. Understanding the dynamics of flow through polymer-grafted nanopores is a next level of complexity in nanofluidics because it involves the interplay of flow field and polymer brush structure in a confined geometry, and because chain collapse can alter pore sizes from those in which prior studies have shown that continuum treatments are appropriate to sizes in which molecular simulations suggest that the Navier-Stokes equation breaks down for non-grafted pores.

In this chapter we explore in detail a continuum fluid dynamics approach for accurately modeling velocity distributions and flow rates through a polymer-grafted nanometer-scale cylindrical pore under both good and poor solvent conditions. Rather than using experimental data, the results of our continuum analysis are compared directly to molecular dynamics (MD) simulations. Because the conditions in the simulations are precisely defined, and the resulting flow characteristics are completely established by the velocities and positions of the flowing particles, this is a stringent evaluation of the continuum approximation for this system.

We consider flow through a cylindrical nanopore modified with polymer chains under an applied flow field F_z along the cylinder axis (Fig. 3.1).

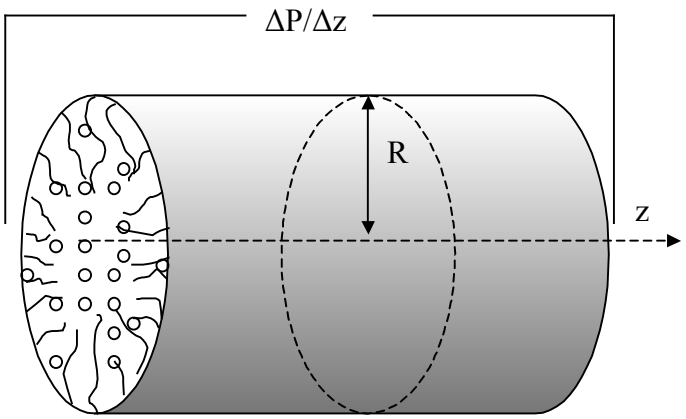

Figure 3.1 Schematic representation of the cylindrical nanopore grafted with polymer chains.

Following earlier continuum calculations [6,10], we treat this problem as flow through a porous medium and approximate the grafted polymers as a brush layer with permeability related to the monomer density. The resulting Brinkman equation [11] for the system can be written as

$$\frac{1}{r}\frac{d}{dr}\left(r\frac{dv_z}{dr}\right)-\frac{v_z}{k}=\frac{1}{\mu}\rho F_z \qquad (3.1)$$

where ρ and μ are the density and viscosity of the solvent, respectively, v_z is the z-component of solvent velocity, and k is the permeability of the brush layer. In principle, this continuum equation can describe flow through a cylindrical nanopore grafted with a polymer brush of a given height by using an infinite k value for the central polymer-free region of the pore (which reduces Eq.(3.1) to the Navier-Stokes equation), and a finite value for permeability through the brush layer that is related to the monomer volume fraction Φ by some function $k(\Phi)$. In practice, however, the accuracy with which flow characteristics can be obtained with a continuum approach has not been established for

these smart materials, nor has an appropriate function for $k(\Phi)$ been derived. These are critical issues both from the viewpoint of the fundamental mechanics of fluid flow in confined systems, and from a technological viewpoint as these systems are developed for wide applications.

3.2 Molecular Dynamics Simulations of Flow in Good and Poor Solvent Conditions

The MD simulation system that was studied consists of polymer chains of length N end-attached to the inside of a cylindrical pore with radius R that is filled with a pool of explicit solvent atoms. The polymer chains, which are grafted at a density of one chain per an area of s, are represented by a bead-spring model. The grafting surface is represented by stationary wall atoms of the same size as the polymer beads placed on a cylindrical surface. Non-bonded interactions between monomer-monomer (mm), monomer-solvent (ms), solvent-solvent (ss), monomer-wall atom (mw) and solvent-wall (sw) atom pairs are modeled using a Lennard-Jones shifted force potential of the form

$$U_{SF}(r_{ij}) = \begin{cases} U_{LJ}(r_{ij}) - U_{LJ}(r_c) - (r_{ij} - r_c)\left(\dfrac{dU_{lj}(r_{ij})}{dr_{ij}}\right)_{r_{ij}=rc} & r_{ij} \le r_c \quad , \\ 0 & r_{ij} > r_c \end{cases} \tag{3.2}$$

where ULJ(rij) is the Lennard-Jones potential given by

$$U_{LJ}(r_{ij}) = 4\varepsilon_{ij}\left\{\left(\frac{\sigma_{ij}}{r_{ij}}\right)^{12} - \left(\frac{\sigma_{ij}}{r_{ij}}\right)^{6}\right\} \tag{3.3}$$

and rc is the cutoff distance beyond which the interaction is zero. The quantities εij and σij are energy and distance parameters, respectively, corresponding to a particular pair of particles i and j. Values of εij =0.5kJ/mol and σij =2.7Ao are used for all pair interactions unless stated otherwise. Neighboring monomers along a chain interact via a harmonic bond potential with the value of spring constant kb=40εmm/σmm and equilibrium distance ro=σmm. The cylindrical nanopore, which has radius R=30σmm and length L=120σmm, is grafted with polymer chains with N=10, s= 100 σmm2. The pore is filled with 142,191 solvent atoms of the same size and mass as the polymer beads. The total number of particles in the system is 187,753 at a reduced number density of 0.5533. A periodic boundary condition is applied along the z-axis, which is parallel to the axis of the cylinder, and a single body external force Fz on each solvent atom generates flow in the z-direction. A constant temperature is maintained by coupling the system to a Nosé-Hoover thermostat. A snapshot of the system from a MD simulation is illustrated in Fig. 3.2.

Figure 3.2 Snapshot from a MD simulation of the polymer grafted cylindrical nanopore. Color-coding: red (fluid atoms), gray (wall atoms) and yellow (polymer).

The MD simulations, which used a time step of 5fs, were performed using the DL_POLY_2.12 code [12]. The structure was equilibrated for $2x10^5$ steps before the external field was switched on. Once the external field was switched on the simulations were carried out for long enough time that the flow was fully developed and the grafted polymer layer responded to the flow. Typically, sampling was begun 5 x 10^5 time steps after switching on the flow field. The solvent velocity profile was generated by calculating the time average of the *z*- component of the velocity of the solvent atoms that are at a distance r from the center of the pore, averaged over $5x10^5$ time steps.

To analyze the system's ability to control flow, MD simulations of fluid flow under two different solvent conditions were carried out. For the good solvent case the truncation distance r_c in Eq.(3.2) for the mm interactions was taken as $2^{1/6}\sigma_{mm}$, which truncates the potential such that only repulsive interactions are included. For the poor solvent case, a cut-off of $2.5\sigma_{mm}$ (which includes the attractive part of the potential) and an interaction potential ε_{mm} =1.0kJ/mol were used for the mm pair. This choice of parameters was made so that the mm interaction was favored over the ms interaction, resulting in the collapse of the grafted chains. Snapshots from MD simulations for the good and poor solvent cases are illustrated in Fig. 3.3. Plotted in the top panel of Fig. 3.4 is the monomer density profile for the good and poor solvent conditions. The monomer density profile is diffuse and extends to the center of the cylindrical pore for a good solvent, and drops off within a short distance of the pore wall in the case of a poor solvent, leaving a central polymer free region. Plotted in the bottom panel of Fig. 3.4 is the average velocity of the solvent atoms as a function of distance *r* from the pore center for an applied force F_z=1.6605x10$^-$

^{3} pN. For the good solvent case the extended chains offer resistance to flow and the flow rate is close to that of a closed pore. In the case of the poor solvent, collapse of the chains increases the pore size, thereby enhancing the overall flow rate to that of an open pore.

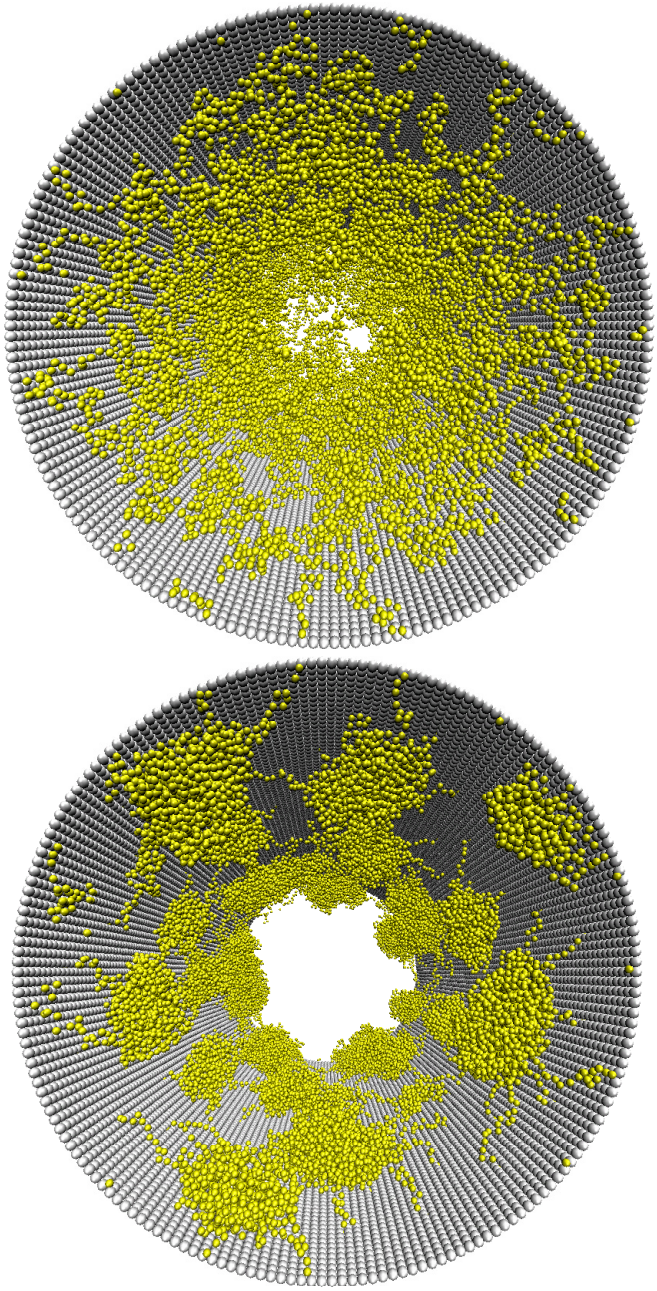

Figure 3.3 Snapshots from the MD simulations of the system under good (top) and poor (bottom) solvent conditions. Fluid atoms are not shown for better visualization.

It is well known from the polymer literature that polymer chains are deformed when subjected to a strong flow. Although shear induced deformation can provide additional mechanism of flow control, in this Chapter we have restricted ourselves to a shear rate regime where there is no change in the brush thickness due to shear deformation. In our simulations we have chosen an external field small enough such that the flow does not deform the chains considerably to cause shear induced thinning of the layer. To determine what shear rate regime does the flow field in our MD simulations fall we have carried out the following analysis. Shear induced thinning is expected in the case of polymer chains in coil conformations (good or theta solvents) when subjected to a shear flow stronger than the entropic restoring force. There are two different characteristic time scales involved. First, the relaxation time of the polymer chain, τ_R, which determines the time required for a fully deformed chain to rearrange back to its equilibrium configuration. The second is defined by the applied strain rate $d\gamma/dt$. When the rate of deformation is faster than the time required for the chain to relax to the equilibrium configuration, one expects stretching of the chain in the flow direction. The strength of the flow field is characterized by the dimensionless Weissenberg number $W_i = \tau_R \, d\gamma/dt$. To determine the relaxation time, an MD simulation of an isolated free polymer chain of length 100 in a pool of solvent atoms was carried out. τ_R was calculated to be approximately 125 ps by fitting to a single exponential the decay of the autocorrelation function of the deviation of the radius of gyration from the mean value. The Weissenberg number for the MD simulations performed was estimated to be 0.05 for the flow field applied. This is well below the range of W_i reported by Doyle *et al*. [13] to produce a

significant deformation of the grafted chains. This analysis is also supported by the fact that monomer density profile for F_z=0.0 and 0.0016605 pN were effectively the same.

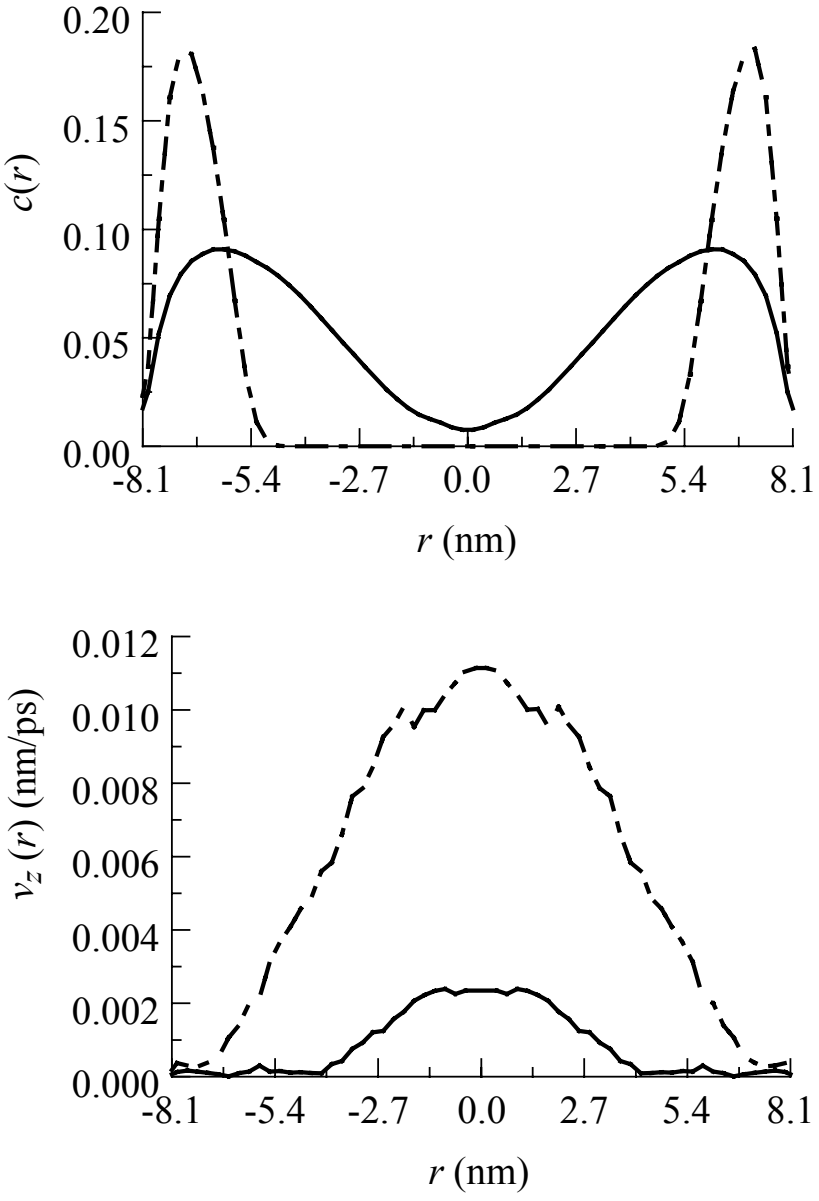

Figure 3.4 Results of the MD simulations. Top: Monomer density (number/σmm3) profile for good (solid line) and poor (broken line) solvents. Bottom: Solvent velocity profile for good (solid line) and poor (broken line) solvents, Fz=1.6605x10-3 pN.

3.3 Comparison of Porous Layer Models

Solving the continuum equation requires an expression that relates $\Phi(r)$ to the permeability k used in Eq.(1). The most obvious choice would be based on the dilute limit model [11,14] where each monomer of diameter a is treated as a spherical obstacle to flow and the permeability through a swarm of beads can be derived by computing the total drag force exerted by the fluid on the beads using Stoke's law [11]. This leads to the expression $k=a^2/18\Phi$. However, this model overestimates the drag force because it assumes that the obstacles are not connected and do not interact with each other. In the case of a polymer brush, monomers of a chain are connected and offer much less resistance to flow as compared to an equivalent volume fraction of uniformly distributed unconnected spheres of the same size. Kim *et al.* [14] made a similar observation that the dilute limit model underestimates the permeability of three-dimensional fractal porous aggregates as only a fraction of particles offer resistance to flow in the case of connected obstacles. As polymer chains are fractals with dimensionality $1/\delta$, where δ is the scaling exponent (= 3/5 for good solvents, ½ for theta solvents and 1/3 for poor solvent), it would be appropriate to consider other models. In the case of good and theta solvents the permeability expression can be derived based on polymer dynamics theories pioneered by de Gennes [15]. For semidilute polymer solutions there exists a correlation length ξ that depends on the polymer concentration ($c= 6\Phi/\pi a^3$) as $\xi= a^{1/1-3\delta}\ c^{\delta/1-3\delta}$. ξ corresponds to the mesh size of the porous network of entangled polymer chains. On the scales below ξ (which is also the blob size) the chains are self-avoiding walks characterized by the scaling law $\xi \sim ag^{\delta}$, with g being the number of monomers per blob. de Gennes noted that in the presence of a localized solvent velocity disturbance the chain segments are able to

follow the flow field for a distance of the order of ξ, beyond which they feel the constraints from the temporary network. Hence, noting that the system studied here falls in the semidilute regime, it is reasonable to assume that it is the blob that acts as the obstacle to flow rather than the monomer. The blob can be envisioned as an obstacle resulting in an expression for permeability, $k= \xi^2=a^2(6\Phi/\pi)^{2\delta/1-3\delta}$.

In the poor solvent case, grafted chains aggregate to form pinned micelles with globular cores and extended legs connecting the core with the grafting point (see bottom panel, Fig. 3.4). The formation of pinned micelles causes inhomogeneity in the monomer density parallel to the grafting surface. The formation of pinned micelles have been proposed by Williams [16] and Zhulina *et al.* [17] in the case of sufficiently dense brushes exposed to a poor solvent. As not all the monomers are exposed to flow it would be more appropriate to consider each pinned micelle as a spherical obstacle to flow in determining the permeability of the layer. In our MD simulations there were on average m=9 chains per micelle, for which the average size can be calculated as $R_m \sim a(mN)^{1/3}$=2.6 nm.

The continuum flow velocity profile was generated in the following fashion. The calculation used as an input $\Phi(r)$ obtained from the MD simulations. Due to the variation of polymer volume fraction as a function of r, Eq.(3.1) must be solved numerically. The calculation was performed by dividing the brush region into n annular shells of thickness dr. The Brinkman equation was written for i =1, n shells separately with permeability value k_i related to $\Phi(r)$ of the corresponding shell. For shells free of polymers Eq.(3.1)

reduces to the Navier-Stokes equation. The solution for the velocity profile involved making an initial guess for the velocity at the center of the pore. Equation (3.1) was then applied to shells i=1 (r=0) to n (r=R) sequentially, subject to boundary conditions of constant velocity and shear stress at the interface between shell i-1 and i to obtain the velocity profile inside the pore. The composite velocity profile across the nanopore was obtained by successively improving the guess until the boundary condition that velocity at r=R vanishes was met. The viscosity of the Lennard-Jones fluid used in the MD simulations was determined by carrying out a set of MD simulations of Poiseuille flow of the fluid through a polymer free cylindrical nanopore. The velocity profile generated was fit to a parabolic profile and the viscosity was estimated from well-known equations of fluid mechanics.

Plotted in the top panel of Fig. 3.5 is the velocity profile from the MD simulations for the good solvent case along with the equivalent profiles calculated by the continuum method using the dilute limit model and the blob model. The dilute limit model underestimates the permeability of the structure whereas the continuum model based on the blob picture agrees well with the MD simulation results. Plotted in the bottom panel of Fig. 3.5 is the continuum velocity profile calculated using the dilute limit model, the pinned micelle model and MD simulation results for the poor solvent case. The pinned micelle model agrees better with the velocity profile from the MD simulations than the dilute limit

model as expected. In the case of polymer brushes the dilute limit model underestimates the permeability in good as well as poor solvents.

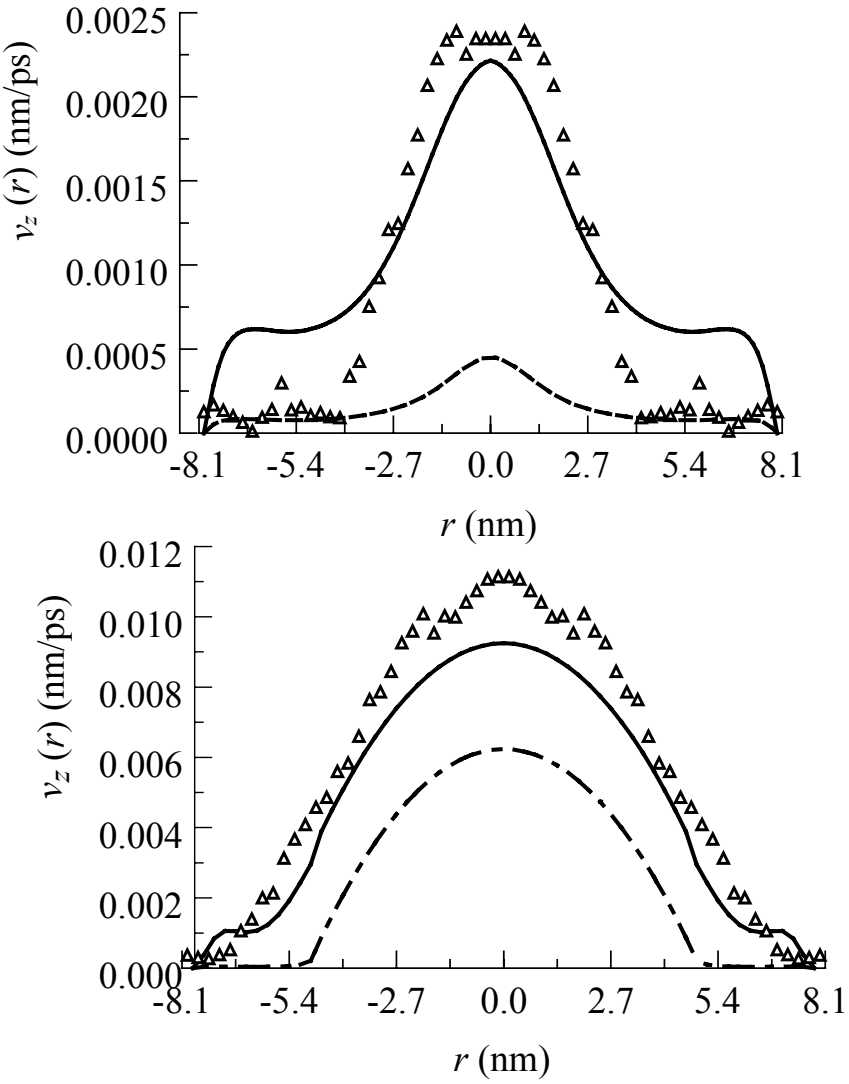

Figure 3.5 Comparison of velocity profiles from MD simulations and the continuum method. The continuum calculations used the Φ(r) from MD simulations. Top: vz(r) from the dilute limit model (broken line), the blob picture (solid line), and MD simulations (triangle) for the poor solvent. F_z=1.6605x10^{-3} pN.

3.4 Design of the Smart Flow Control Valve Using Continuum Method

With the appropriate porous layer model to be used in the continuum calculations established, the continuum equations can be used to efficiently characterize nanoporous systems for their ability to control flow over a range of solvent quality. This requires that the monomer volume fraction distribution be known at different values of solvent quality. To calculate this distribution for a general case, we have extended the mean field analytic theory of Zhulina and co-workers [18] developed for planar brushes to the case of a concave cylindrical brush. Let us consider polymer chains of length *N* beads grafted to an impermeable concave cylindrical surface of radius *R*, with a grafting density of one chain per an area of *s*. Polymer bead size is chosen to be a. Let *r* be the radial distance measured from the axis of the cylinder and *h*=*R*-*r*, be the distance from the grafting surface.

The equilibrium monomer density profile or alternatively monomer volume fraction as a function of distance from grafting surface, $\phi(h)$, in the brush layer can be determined by minimizing its total conformational free energy,

$$\Delta F = \Delta F_{conc} + \Delta F_{el} \tag{3.4}$$

which contains the volume interaction energy,

$$\Delta F_{conc} = \frac{s}{a^3 R}\int_0^H \upsilon\phi^2(h)(R-h)dh \tag{3.5}$$

and elastic stretching energy

$$\Delta F_{el} = \int_0^H g(h')dh' \int_0^{h'} E(h,h')dh \tag{3.6}$$

where the function g(h') is the average fraction of chains ending at a radial distance h' and E(h, h') gives the local stretching dh/dn at h for a chain ending at h'. The solvent quality is characterized by the excluded volume parameter

$$\upsilon = \frac{1}{b_0}\int 2\pi r^2 \left[1 - \exp\left(-\frac{U(r)}{k_B T}\right)\right] dr \tag{3.7}$$

where $U(r)$ is the monomer-monomer interaction potential, k_B is the Boltzmann constant, T is the temperature and $b_0=2\pi\sigma_{mm}^3/3$. The volume fraction of monomers $\phi(h)$ is expressed by the functions $g(h')$ and $E(h, h')$ as

$$\phi(h) = \frac{a^3 R}{s(R-h)} \int_h^H \frac{g(h')}{E(h,h')} dh' \tag{3.8}$$

Minimizing the free energy ΔF as a functional of unknown functions $g(h')$ and $E(h, h')$ under the constrains

$$\frac{s}{a^3 R}\int_0^H \phi(h)(R-h)dh = N \tag{3.9}$$

and

$$\int_0^{h'} \frac{1}{E(h,h')} dh = N \tag{3.10}$$

gives the expression for the function of local chain stretching

$$E(h,h') = \frac{\pi}{2N}\sqrt{h'^2 - h^2} \tag{3.11}$$

and for volume fraction of monomers in a layer

$$\phi(h) = \frac{1}{2\upsilon}(-K^2h^2 - \lambda) \tag{3.12}$$

where

$$K^2 = \frac{3\pi^2}{8N^2a^2} \tag{3.13}$$

and λ is a undetermined Lagrangeian multiplier that can be determined from normalization of Eq.(3.9). The function $g(h^{'})$ can then be be determined by solving the integral Eq.(3.8), with $g(h^{'})$ as an unknown function.

Eqs (3.11), (3.5) and (3.6) were used to determine the free energy ΔF as a function of height H. The equilibrium value of brush height, H_0 was determined by minimizing the free energy with respect to H. Once H_0 is known, the monomer volume fraction profile is easily computed.

The analysis of the system's ability to control flow is carried out by varying υ to obtain the equilibrium $\Phi(r)$ and solving the Brinkman equation to determine the velocity profile using the method described above. Plotted in the top panel of Fig.(3.6) is the flow rate $Q = \int_0^R 2\pi r v_z(r)dr$ as a function of υ for an applied external field F_z = 1.6605x10^{-3} pN. The decrease in flow rate is about four times from υ=0 to 1.0. In principle, the smart nanopore can be designed to have any desired ratio of flow rate in open and closed configuration by choosing an appropriate pore radius and polymer content P_c (the amount of grafted polymer per unit pore volume = $2N/sR$). It can be noted from the bottom panel of Fig. 3.6

that for a given pore radius increasing the polymer content enhances the selectivity (Q_{open}/Q_{closed}) of the nanopore.

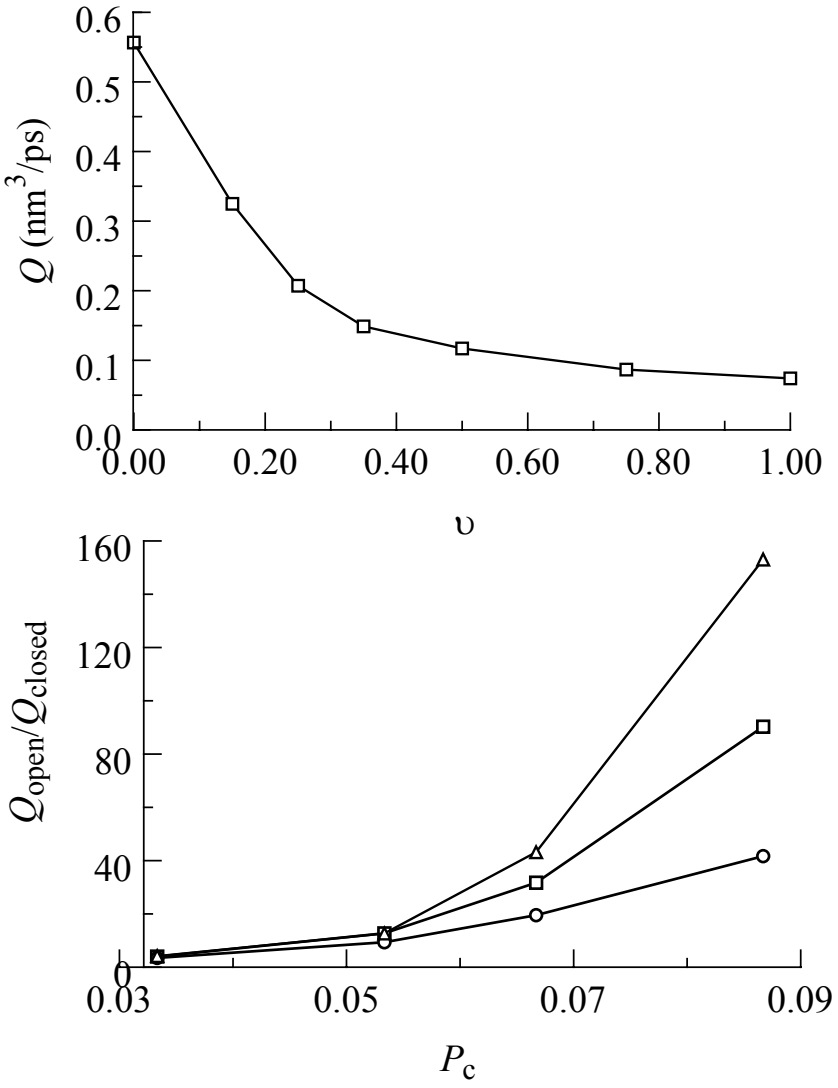

Figure 3.6 Results from continuum calculations. Top: Variation of flow rate with solvent quality as calculated from the continuum method for R/σ_{mm}=30, polymer content P_c=0.0667. The Φ(r) was calculated from mean field theory at each value of υ. Fz=1.6605x10-3 pN. Bottom: Ratio of Q at open (υ=0.0) and closed (υ=1.0) conditions as a function of P_c at three different values of pore radius R/σ_{mm}=60 (circles), 90 (squares) and 120 (triangles).

3.5 Summary

In this chapter we have investigated solvent flow through a polymer grafted cylindrical nanopore with respect to its ability to control flow in response to change in solvent quality. Using md simulations we showed that the system is capable of changing the permeability drastically upon changing the solvent quality from good to poor. We have demonstrated that continuum fluid dynamics using a porous layer model is capable of accurately describing flow through polymer grafted nanopores provided that an appropriate permeability expression based on polymer layer structure and dynamics is used. This result establishes a critical starting point from which modeling can be used to design smart nanoporous materials with tailor-made properties. The application of the method described here can be extended to any specific polymer-solvent system assuming that monomer density profile can be computed as a function of solvent quality (i.e. triggering mechanism such as pH, temperature and ion concentration).

References

[1] Y. S. Park, I. Toshihiro, and Y. Imanishi, Langmuir **16,** 5376 (2000).

[2] S. Akerman *et al.* Int. J. Pharma. **164**, 29 (1998).

[3] A. M. Mika, R. F. Childs, and J. M. Dickson, J. Membr. Sci. **153,** 45 (1999).

[4] H. Iwata, I. Hirata, and Y. Ikada, Macromolecules **31**, 3671 (1998).

[5] R. P. Castro, Y. Cohen, and H. G. Monbouquette, J. Membr. Sci. **115**, 179 (1996).

[6] R. P. Castro, H. G. Monbouquette, and Y. Cohen, J. Membr. Sci. **179**, 207 (2000).

[7] J. Koplik, J. R. Banavar, and J. F. Willemsen, Phys. Fluids A **1**, 781 (1989).

[8] K. P. Travis, B. D. Todd, and D. J. Evans, Phys. Rev. E **55**, 4288 (1997).

[9] K. P. Travis, and K. E. Gubbins, J. Chem. Phys. **112**, 1984 (2000)

[10] S. T. Milner, Macromolecules **24**, 3704 (1991).

[11] H. C. Brinkman, Appl. Sci. Res. **A1**, 27 (1947).

[12] DL_POLY is a package of molecular simulation routine written by W. Smith and T. R. Forester, copyright The Council for the Central Laboratory of the Research Councils, Daresbury Laboratory at Daresbury, Nr. Warrington (1996). For details see http://www.dl.ac.uk/TCSC/Software/DL_POLY/main.html

[13] P. S. Doyle, B. Ladoux, and J. Viovy, Phys. Rev. Lett. **84**, 4769 (2000).

[14] A. S. Kim and K. D. Stolzenbach, J. Coll. Int. Sci. **253**, 315 (2000).

[15] P. G. De Gennes, Macromolecules, **9**, 587, (1976).

[16] D. R. M. Williams, J. Phys. II **3**, 1313 (1993).

[17] E. B. Zhulina *et al.* Macromolecules, **28**, 8612 (1995).

[18] Y. B. Zhulina, V. A. Pryamitsyn, O. V. Borisov, Poly. Sci. U.S.S.R. **31**, 205 (1989).

4 pH-Responsive Flow Control through Poly-(L-Glutamic Acid) Grafted Nanoporous Membrane

4.1 Introduction

Conformational transitions in polypeptides have been a subject of extensive research among biologists. These conformational transitions can be induced by a variety of stimuli including temperature, pH and ionic concentration. Motivated by the structure-function of biomolecules, a variety of nanostructures based on conformational transitions of polypeptide molecules have been envisioned. Recently, Park *et al*. demonstrated a pH responsive nanometer scale gate where a polypeptide brush was grafted on to a gold plated porous membrane. The water permeation through the porous material was regulated by a helix-coil transformation of the grafted poly-(glutamic acid) (PLGA) chains in response to pH [1]. A pH-responsive flow control valve is of particular interest in smart drug delivery systems. For example, these polypeptide grafted nanochannels could be used for controlled delivery of insulin in diabetes patients. These systems can be coupled with glucose oxidase that can be immobilized within the drug delivery system. The glucose-glucose oxidase reaction causes lowering of the pH in the microenvironment of the delivery system. This can cause coil-helix transition of grafted PLGA to increase insulin release. One could think of the proposed nanoporous materials as smart molecular gates that open up in response to enhanced levels of blood glucose and release insulin, which is a tiny protein of 51 amino acid residues.

The flow control valve reported by Park *et al.* bases its responsive permeability on the change in thickness of the grafted polypeptide layer in response to a change in pH. At a low pH PLGA has a helical conformation that expands to a random coil conformation as the pH is increased, reducing the effective pore diameter (Fig. 4.1). The thickness of the polypeptide layer as a function of pH is determined by extending the helix-coil transition models developed for biopolymers. A brief review of helix-coil transition in polypeptides is presented in the beginning of the chapter. The theory is used to calculate the thickness of a grafted PLGA layer as a function of pH. We then calculate the change in permeability of a PLGA grafted cylindrical nanopore as a function of pH using the continuum method described in the previous chapter. The results are compared with experiments of Park and coworkers.

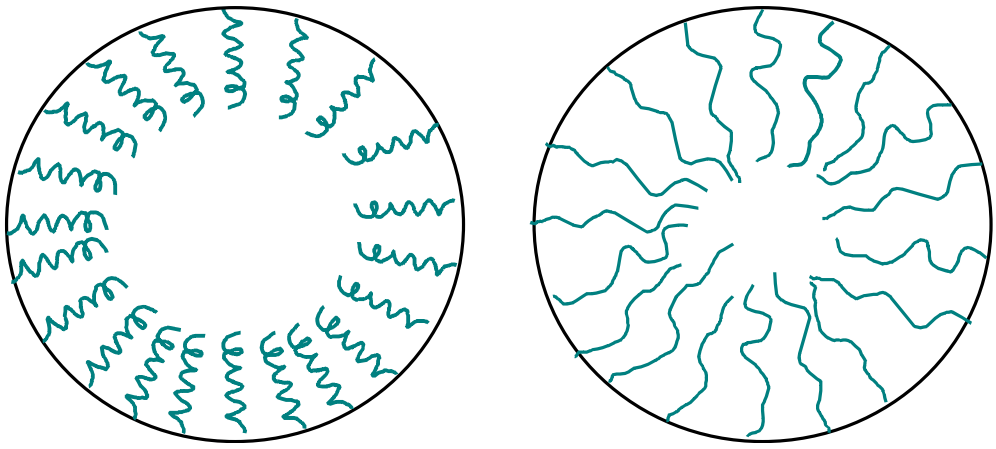

Figure 4.1 Schematic representation of the smart nanopore. At a low pH the PLGA chains are in a helical configuration (left) and at a high pH the chains attain a random coil configuration (right).

4.2 Background

The helix-coil transition in polypeptides has been extensively studied due to their importance in biology [2]. The alpha-helical configuration is characterized by hydrogen bonding between the carbonyl oxygen of the i^{th} residue and the amide hydrogen of the $i+4^{th}$ succeeding residue. This means that the rotation angles, φ and ψ for each of the three successive residues must adopt the required values for an alpha-helix configuration before a hydrogen bond is formed. The helix-random coil transition occurs due to the fact that the alpha helix is favorable energetically because of intramolecular hydrogen bonding, while the random-coil configuration is favorable entropically because of its flexibility [3]. Therefore, the free energies of these two states vary differently with temperature. As the temperature is increased the entropic contribution to free energy dominates and a random-coil state is favored. The helix-coil transition temperature occurs at the point at which the free energies of the two states are identical. These transitions occur within a narrow, finite, temperature interval.

In the case of polypeptide chains with ionizable side-chains, a helix-coil transition can also be brought about by a change in pH. For example, PLGA, which has a carboxylic acid side-chain, is protonated (neutral charge) at a low pH and is deprotonated (negatively charged) at a high pH. In the protonated state, the alpha-helical structure is favored as compared to a random-coil configuration. In the deprotonated state, the Coulombic repulsion between the negatively charged side-chains destabilizes the helical structure and a random-coil is favored. In other words, the helix-coil transition of PLGA

is controlled by neutral-ionic transition of carboxylic side-chains that is driven by a pH change.

The helix-coil transition can be characterized by the fraction of residues *f* in a polypeptide chain that has helical configuration, i. e. those with φ and ψ values corresponding to a helical configuration. In the Zimm-Bragg model, the helix-coil transition is described by two parameters: $s = \exp(-\Delta F/k_B T)$ and $\sigma = \exp(-\Delta F_{init}/k_B T)$ [2,4]. The propagation parameter *s* is associated with adding a helical unit to an already existing helical region. Here ΔF is the free energy change of a monomer unit accompanying its transition from the free state to the helical state (energy gained due to hydrogen bonding). The initiation parameter σ reflects the entropy cost of initiating a helical region. The fact that initiation of a new helical region requires three monomer units to be fixed in a helical configuration as compared to the propagation of an already existing helical region that requires fixation of only one monomer segment costs extra entropy ΔF_{init}. An addition of a monomer to an already existing helical region contributes one hydrogen bond and costs entropy due to fixation of one monomer unit, while initiation of a helical region of *m* monomers contribute *m*-2 hydrogen bonds and costs entropy of fixation of *m* monomer units. In other words, the presence or absence of a helical conformation in the neighboring monomer units strongly influences the formation of a hydrogen bond in one of the monomer units. For this reason σ is also a measure of cooperativity of the helix coil transition. The degree of cooperativity determines the average number of monomer units in a helical section in the middle of a helix-coil transition region, which is equal to [5],

$$\nu = \exp\left(\frac{F_{init}}{2k_B T}\right) = \frac{1}{\sqrt{\sigma}} \qquad 4.1$$

From the Zimm-Bragg model, the helical content is given in terms of the above parameters as

$$f = \frac{1}{2}\left(1 + \frac{s-1}{((s-1)^2 + 4\sigma s)^{1/2}}\right) \qquad 4.2$$

The helix-coil transition in terms of helical content as a function of pH has been investigated both experimentally and theoretically. The experimental methods used for determining the helical content include circular dichroism (CD) and ellipsometry [5]. Zhang *et al*. have applied an electrostatic model to theoretically determine the effect of pH and salt concentration on the helix content of PLGA chains within the Zimm-Bragg formalism [6].

4.3 Molecular Dynamics Simulations of Protonated and Deprotonated Poly(L-Glutamic Acid) Chains

Molecular dynamics (MD) simulations were carried out to extract chain parameters of isolated PLGA molecules in water. Two systems corresponding to PLGA in the protonated ($PLGA_p$) and deprotonated ($PLGA_{dp}$) states were studied using MD simulations. Each system consisted of an 80-residue long PLGA chain, of which the N-terminus and C-terminus were acytylated and methyl-amidated, respectively. The all-atom parameterization of the AMBER force field was used in the simulations. The initial model of the chain was built using the LEAP module of Amber7 [7]. The residues GLH and GLU corresponding to the protonated and deprotonated states, respectively, are included in the Amber library. The $PLGA_p$ chain consisted of all protonated residues and the $PLGA_{dp}$ chain consisted of all deprotonated residues. The completely stretched initial

model of the chain was energy-minimized for 2000 steps to remove any unfavorable contacts between atoms. The minimized structure was then immersed into a box of water molecules having a density of 1 g/cm^3. TIP3P water was used as the water model. Monovalent counter ions (Na^+) were included such that the net charge of the system was zero. The numbers of counter ions included were 2 and 80 for $PLGA_p$ and $PLGA_{dp}$ systems respectively. A time step of 1.0 fs was used in the simulations. The systems were equilibrated at a temperature of 300K for about 50 ps. This was followed by a MD simulation of 1.5 ns. Sampling was begun after 500 ps.

The $PLGA_p$ chain formed a predominantly helical (>85% residues in the helical state) structure. It is reported in the literature that PLGA does not reach 100% helical content even at saturation pH at room temperature. As was expected, the $PLGA_{dp}$ chain formed a random coil. The persistence length of the coil was calculated to be ~ 10 residues, using the method described in Flory's book [8]. The $PLGA_p$ (top panel) and $PLGA_{dp}$ (bottom panel) chains are represented by ribbon models in Fig. 4.2.

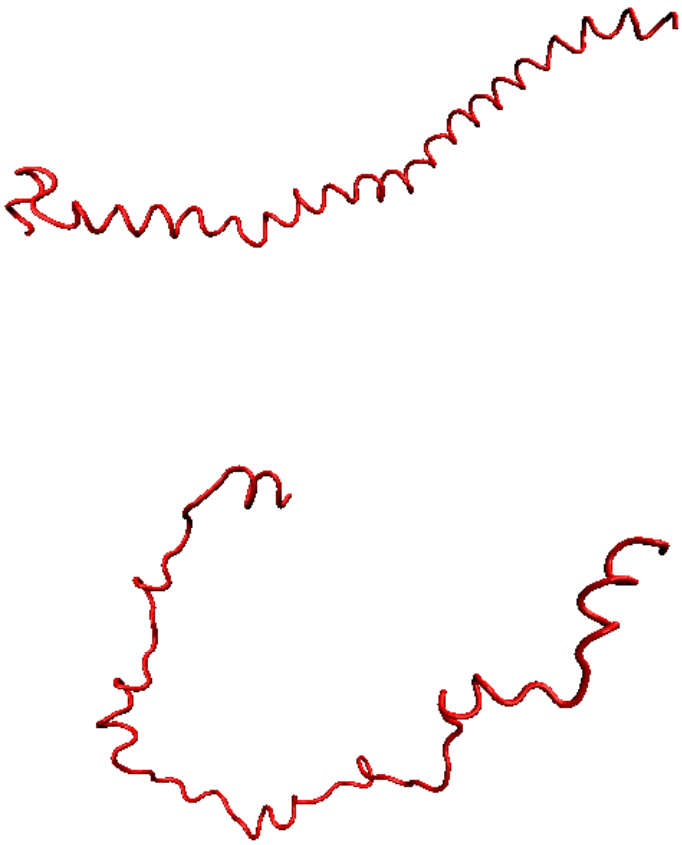

Figure 4.2 Ribbon models of protonated (Top) and deprotonated (Bottom) poly (L-glutamic acid) chains generated from MD simulations. N=80.

4.4 Grafted Layer Thickness as a Function of Helical Content

In this section determination of the PLGA layer thickness as a function of the fraction of helical units (*f*) is described. An exact treatment of the effect of *f* on the layer thickness and morphology is overwhelming. However, the dependence of monomer density distribution on *f* in the helix-coil transition region can be analyzed based on the simple model by Nagai and Ptitsyn [2,5] that describes the variation of the dimension of an

isolated chain as a function of *f*. This model considers a chain consisting of the helical and random coil sections that are freely linked to one another. A residue in a helical conformation has a length of l_h=1.5 A^o in the direction of the helix axis. A helical segment in the chain has an average length of v_h residues, i.e. persistence length $L_h = v_h l_h$. For the random coil section, the corresponding parameters are l_c=3.8 A^o and $L_c = p_c l_c$. In a *N* residue long chain there are *fN* residues in the helical conformation and (1-*f*)*N* residues in the random coil configuration. The mean square end-to-end distance (<r^2>) of the chain is given by the sum of mean square end-to-end distances of two hypothetical chains consisting only of coiled sections ((1-*f*)*N* residues) or only of helical sections (*fN* residues) as follows,

$$\left\langle r^2 \right\rangle = (1-f)Np_c l_c^2 + fNl_h^2 \frac{1+\left\langle \cos\theta \right\rangle}{1-\left\langle \cos\theta \right\rangle} \quad , \qquad 4.3$$

where <cosθ > is the mean value of the cosine of the angle between end-to-end vectors of two helical monomer units. The value of <cosθ > assumes 1 or 0 for monomers in the same helical section or different helical sections, respectively. Therefore, <cosθ > =1x(1-*p*)+0x*p* = 1 – *p*, where *p* is the probability of breaking the helix. *p* is related to the average number of monomer units in a helical section as $v_h = 1/p$. Following Ptitsyn [5], the following expression for the mean square end-to-end distance can be derived:

$$\left\langle r^2 \right\rangle = N\left((1-f)p_c l_c^2 + 2fl_h^2 \nu \sqrt{\frac{f}{1-f}} \right) \qquad 4.4$$

The monomer density profile in the grafted layer was calculated using the mean field approximation described in section 3.4. The method needs as input a repeat length of monomer units and the persistence length parameter. A chain in the helix-coil transition region with both helical and random-coil units can be represented by a hypothetical chain

that has an effective repeat length a_{eff} and an effective persistence length parameter p_{eff} and hence,

$$\left\langle r^2 \right\rangle = N p_{eff} a_{eff}^2 \qquad 4.5$$

Approximating the value of a_{eff} as the weighted average of helical and random coil repeat lengths, i.e. $a_{\text{eff}} = (1\text{-}f)\, l_c + f l_h$, p_{eff} can be determined by solving Eq. (4.4) and Eq. (4.5). In our calculations a value of p_c = 10 as determined from MD simulations was used. For PLGA, the average number of monomers per helical section in the middle of the transition region is reported in the literature to be v=15. Using these values we have calculated the monomer density profile for a PLGA grafted inside a cylindrical nanopore of radius R=80 nm as a function of f. The values N=80 and a grafting density =0.05 l_c^{-2} were used. The monomer density c(r) plotted in the top panel of Fig. 4.3 for different values of f shows spreading of the grafted layer as the helical content is decreased. This indicates that for the brush considered in the calculation increasing f increases the pore opening. This is better illustrated by a plot of effective brush thickness defined as,

$$H = \frac{\int rc(r)dr}{\int c(r)dr}, \qquad 4.6$$

in the bottom panel of Fig. 4.3.

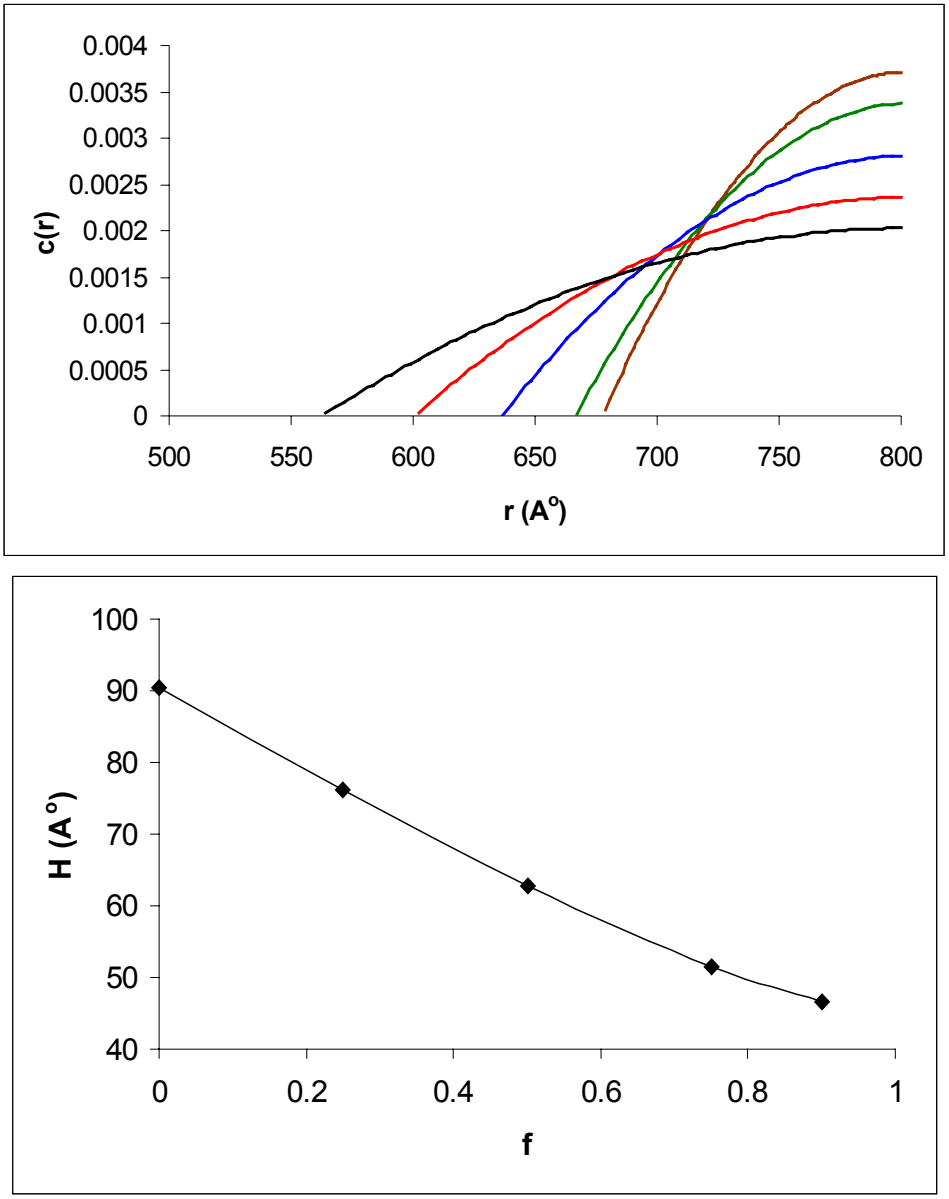

Figure 4.3 Results from mean-field calculations. Top: Monomer density (number/σmm3) profile for f=0.9 (brown), 0.75 (green), 0.5 (blue), 0.25 (red), and 0 (black). R is the distance from the center of the pore. Bottom: Variation of brush thickness with f. R=80 nm, N=80, grafting density=0.05 l_c^{-2}.

4.5 pH-Sensitive Flow Control – Analysis of Park, Ito and Imanishi's Experiments

In their experiments, Park *et al*. measured a change in water permeability through a PLGA grafted nanoporous membrane as a function of pH. The track etched porous polycarbonate membrane had an average pore diameter of 200 nm. The membrane was first coated with platinum and followed by gold. The thickness of the total coated metal was reported as 20 nm. Therefore we use a pore radius R = 80 nm in our calculations. PLGA chains of length N = 80 or 480 residues, carrying a disulphide group at the N-terminal, were self-assembled on the metal-coated surface. The amount of PLGA (N=80) and PLGA (N=480) was 6 x 10^{-11} and 4 x 10^{-11} mol/cm^2 respectively. This corresponds to a distance between grafting points of 1.6 and 2.1 nm for N=80 and N=480 respectively.

To compare the predictions of our model with the permeation experiments we used f at different pH values reported in the literature [6]. c(r) was obtained for the N=80 PLGA system at various pH values. Then the Brinkman equation was solved to obtain the flow rate through the nanopore as a function of pH. In Fig. 4.4 we have compared the normalized flow rate Q/Q_0 as computed by the continuum analysis and Park and coworkers' experiments. Here Q_0 is the flow rate through an unmodified pore of the same diameter. Results from our model predict a slightly lower flow rate than the experimentally reported value throughout the pH interval of the analysis. However, the model agrees with experiments qualitatively very well with the data. This discrepancy between the results is reasonable considering the uncertainties in the parameters that correspond to the experiments. For example, the pore radius used in our calculation

corresponds to the average pore radius of the membrane subtracted by the thickness of the coated metal layer, the estimated value of which was reported to be 20 nm.

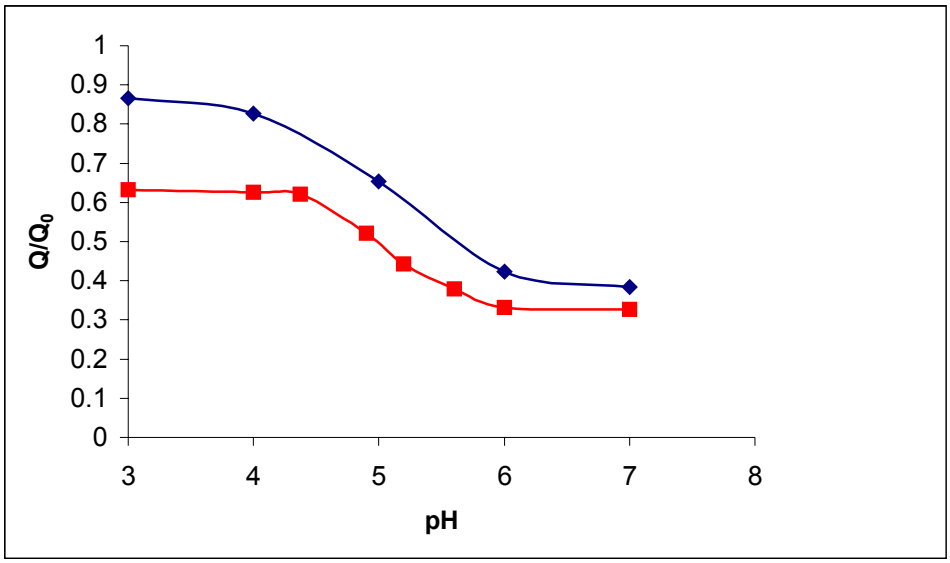

Figure 4.4 Comparison of results from continuum model and experiments. Plotted is the normalized flow rate as a function of pH from theory (red) and experiment (blue) [1].

4.6 Summary

In this chapter, the continuum method based on the Brinkman equation, described in the previous chapter, is applied to analyze water permeation control through a nanoporous membrane grafted with poly-L-glutamic acid chains. We have analyzed the helix-coil transition according to the Zimm-Bragg model to determine the thickness of the grafted polypeptide layer inside a cylindrical nanopore as a function of pH. We have then calculated the flow rate through the nanopore as a function of pH. The results are compared with recent experiments by Park and coworkers [1]. Results obtained from the highly simplified model were in qualitative agreement with experimental water

permeability reported. The results further establish that polymer statistical mechanical models combined with a continuum porous layer treatment of flow through the polypeptide grafted nanopore can be used successfully to design smart flow control systems.

References

[1] Y. S. Park, I. Toshihiro, and Y. Imanishi, Langmuir **16,** 5376 (2000).

[2] D. Poland, and H. A. Scheraga, Theory of Helix-Coil Transitions in Biopolymers, Academic Press, New York (1970).

[3] T. M. Birshtein, and O. B. Ptitsyn, Conformations of Macromolecules, Interscience Publishers, New York (1966).

[4] A. Y. Grosberg, and A. R. Khokhlov, Statistical Physics of Macromolecules, AIP Press: New York (1994).

[5] G. N. Ramachandran, Ed. Conformation of Biopolymers, Academic Press, New York (1967).

[6] W. Zhang, and S. Nilsson, Macromolecules, **26**, 2866 (1993).

[7]. D.A. Case, D.A. Pearlman, J.W. Caldwell, T.E. Cheatham III, J. Wang, W.S. Ross, C.L. Simmerling, T.A. Darden, K.M. Merz, R.V. Stanton, A.L. Cheng, J.J. Vincent, M. Crowley, V. Tsui, H. Gohlke, R.J. Radmer, Y. Duan, J. Pitera, I. Massova, G.L. Seibel, U.C. Singh, P.K. Weiner and P.A. Kollman (2002), AMBER 7, University of California, San Francisco.

D.A. Pearlman, D.A. Case, J.W. Caldwell, W.S. Ross, T.E. Cheatham, III, S. DeBolt, D. Ferguson, G. Seibel, and P. Kollman. AMBER, a package of computer programs for applying molecular mechanics, normal mode analysis, molecular dynamics and free energy calculations to simulate the structural and energetic properties of molecules.

Comp. Phys. Commun. **91,** 1 (1995).

[8] P. F. Flory, Statistical Mechanics of Chain Molecules, Hanser Publications: New York (1969).

5 Virtual Molecular Design of a Comb Polymer Grafted Environment-Responsive Nanoporous System

5.1 Introduction

Materials that contain pores of molecular size have a variety of applications including filtration, size-sorting biomolecules and chemical separation. The conventional transport selectivity of such materials is based on features such as charge, chemical interaction and molecular size. Recent experiments by Park, Ito and Imanishi [1] have shown that additional selectivity can be built into nanoporous materials such that signal responsive liquid permeation is achieved. In one set of experiments, the permeation of toluene through pores in a glass filter was controlled by UV/visible irradiation that induces a collapse transition in a polymer brush. In this experiment, a polymer brush was made by grafting a spiropyran-substituted methyl methacrylate/ methyl methacrylate copolymer on to a glass filter. The optically active functional group associated into the polymer chains formed a stable Zwitterion upon UV irradiation, while the uncharged structure was recovered by irradiation with visible light in combination with heat. Toluene acts as a good solvent for the brush in its uncharged state, but a poor solvent when the brush contains Zwitterions. Hence the brush swells in its uncharged state in toluene, filling the pores and significantly reducing the flow of toluene. In the charged state the brush collapses, opening the pores and allowing solvent flow. In a second set of experiments [2] polypeptide brushes were self-assembled onto a gold plated nanoporous membrane. The

permeability of water was controlled via a helix-coil transformation that was driven by solvent pH.

Motivated by the experiments of Park, Ito and Imanishi, we have been using molecular simulations to explore the functionality of other systems that could potentially act as smart molecular valves. The design discussed here is based on a rod-globule transition in polymer comb molecules. Polymer comb molecules, also termed brush polymers or molecular bottlebrushes, consist of densely grafted side-chains extending from a polymer backbone. Comb polymers can be either copolymer or homopolymer macromolecular structures. For example, polymacromonomers based on polystyrene and poly- (2-vinylpyridine) side chains grafted on a methacrylate backbone are known to form a cylindrical brush [3] The excluded volume interaction of the side chains causes stretching of the main chain such that it adopts a cylindrical brush structure. Depending on the length and density of the side chains, and the interaction between them, comb polymers can attain very high stiffness [4] Kuhn statistical segment length of the order of 1000 A^{o}. In a poor solvent a comb polymer can undergo a conformational transition. In a molecule with a flexible backbone, collapse of the side chains will result in axial contraction of the whole molecule and may result in a globular state as compared to a fully stretched cylindrical brush in a good solvent [5].

In the proposed structure polymer brush molecules are grafted to the interior of a slit nanopore (Fig. 5.1). In the presence of a good solvent the grafted comb molecules are stretched away from the grafting surface, forming a network of obstacles for molecular

diffusion through the pore. Upon exposure to a poor solvent the polymer comb molecules undergo a collapse transition, leaving the pore open, thereby reducing resistance to diffusing molecules. In principle, by a proper selection of solvent-polymer comb combination one can design a molecular gating system that can be opened and closed by varying the solvent quality. Attachment of comb polymer molecules has the potential advantage over linear polymer chains like those used in the Park, Ito and Imanishi experiment with the gold-covered nanoporous membrane in that comb molecules might form a more effective network of obstacles for screening large molecules.

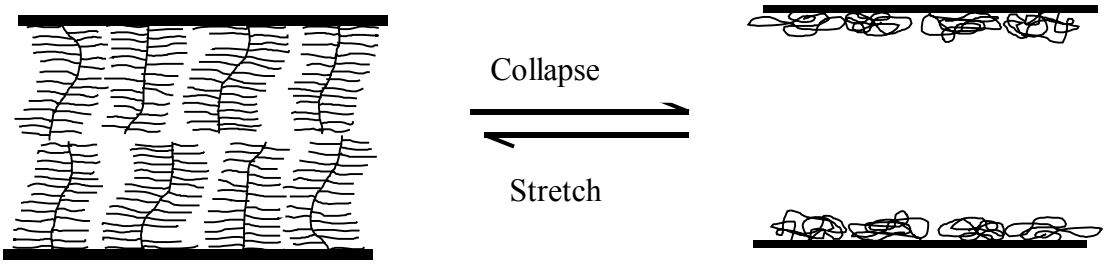

Figure 5.1 Illustration of the proposed nanoporous system.

The feasibility of the proposed system depends on several factors. These factors include the time required to respond to stimuli, the volume difference between the extended and globule state of the grafted chains, the range of stimuli over which the chains respond (e.g. the temperature range for a thermal transition), and the efficacy of the system for inhibiting flow of solute molecules depending on their size. A bead-spring molecular model has been used to explore these factors, with the main objective being to provide a proof-of-concept for the proposed nanoporous system. The first part of this Chapter discusses the nature of the rod-globule transition in an isolated polymer brush molecule as predicted by the model, including the difference in volume between the two states, the

time scale associated with the transition, and the order of the transition. In the second part of the Chapter, opening and closing of the pore by the grafted system and transport of chain molecules through this nanopore as a function of solvent quality is modeled.

5.2 Method

The simulations were carried out using the DL_POLY_2.12 molecular dynamics code [6]. The polymer brush molecules were simulated using a bead-spring model [7] with the mass of each bead taken as 14 AMU. Non-bonded pair interactions, which were included between all pairs of beads except the nearest neighbors, were modeled using a Lennard-Jones shifted force potential of the form

$$U_{SF}(r_{ij}) = \begin{cases} U_{LJ}(r_{ij}) - U_{LJ}(r_c) - (r_{ij} - r_c)\left(\dfrac{dU_{lj}(r_{ij})}{dr_{ij}}\right)_{r_{ij}=rc} & r_{ij} \le r_c \quad , \\ 0 & r_{ij} > r_c \end{cases} \tag{5.1}$$

where $U_{LJ}(r_{ij})$ is the Lennard-Jones potential given by,

$$U_{LJ}(r_{ij}) = 4\varepsilon_{ij}\left\{\left(\frac{\sigma_{ij}}{r_{ij}}\right)^{12} - \left(\frac{\sigma_{ij}}{r_{ij}}\right)^{6}\right\}, \tag{5.2}$$

and r_c is the cutoff distance beyond which the interaction is zero. The quantities ε_{ij} and σ_{ij} are the respective energy and distance parameters corresponding to the particular pair of particles i and j. Values of ε_{ij} =0.5kJ/mol and σ_{ij} =2.7A^o were used for all pair interactions (unless stated otherwise). The truncation distance r_c in Eq. (5.1) for the non-bonded interactions was taken as either $2^{1/6}\sigma$ or 2.5σ. The former distance truncates the

potential such that only repulsive interactions are included, while the latter allows attractive forces to be modeled. Neighboring monomers along a chain interact via a harmonic bond potential with the value of spring constant $k=40\varepsilon/\sigma$ and equilibrium distance $r_o=\sigma$.

The molecular dynamics simulations used a timestep of 5fs and unless otherwise stated were carried out at constant energy. Each system was initially equilibrated for a minimum of 5 x 10^4 time steps during which velocities were scaled to obtain the desired temperature. After equilibration data was typically obtained over runs of 10^5-10^6 time steps. The size of a polymer chain consisting of N monomers is defined using the mean square end-to-end distance,

$$\left\langle R^2 \right\rangle = \left\langle \left(R_N - R_1\right)^2 \right\rangle, \tag{5.3}$$

where R_N and R_1 are coordinates of monomer N and 1 respectively, and the mean square radius of gyration,

$$\left\langle R^2{}_g \right\rangle = \frac{1}{N}\sum_{i=1}^{N}\left\langle \left(R_i - R_{COM}\right)^2 \right\rangle \tag{5.4}$$

where R_i is the coordinate of monomer i, R_{COM} is the coordinate of center of mass of the molecule, and the brackets indicate an average over the equilibrium dynamics of the system. Radii referred to below correspond to either the entire molecule or just the backbone monomers.

5.3 Collapse Transition in Isolated Comb Molecules

The equilibrium size of a comb polymer molecule depends on the number of monomers in the main chain *N*, the number of monomers along the side chain *n*, the number of monomers between subsequent side-chains *m*, and the type of solvent. For example, Rouault and Borisov [8] have used free energy calculations to estimate the equilibrium size of the main chain and the side chains in a good solvent. The relation,

$$R \cong N^{3/5} a \left(1 + \frac{n}{m}\right)^{2/5} \tag{5.5}$$

where *a* is the monomer size, indicates that the effective size of a polymer brush molecule can be tuned by changing the size and grafting density of the side chains. Poor solvent conditions, either due to a reduced temperature or the presence of a solvent with relatively less affinity, can induce a collapse transition to a globule structure in these molecules. In the globular state, it is expected that the brush size R, including the side chains and the backbone, will scale as

$$R \cong \left[N \left(1 + \frac{n}{m}\right) \right]^{1/3} a \tag{5.6}$$

where *N*, *n* and *m* are as above. From the above equations the size change associated with a rod-globule transition can be easily estimated. For example, the radius of a comb polymer with *N*=200, *n*=40 and *m*=4 will be reduced by about 50% upon collapse.

To characterize the nature and timescale of the transition, isolated polymer brush molecules consisting of *N*=200 monomers in the backbone and *n*=40 monomers along the

side chains with spacer length m=2, 3, 4 and 6 were simulated. All nonbonded interactions involving the backbone monomer pairs (i.e. backbone-backbone and side chain-side chain) were taken to be purely repulsive, while an attractive nonbonded interaction was included between monomers in the side chains. The simulations indicate that the comb polymer model undergoes a rod-globule transition that depends on temperature. Illustrated in Fig 5.2 are typical snapshots of stretched and collapsed comb polymers. Plotted in Fig. 5.3 is the radius of gyration of the whole molecule as a function of temperature for different values of m.

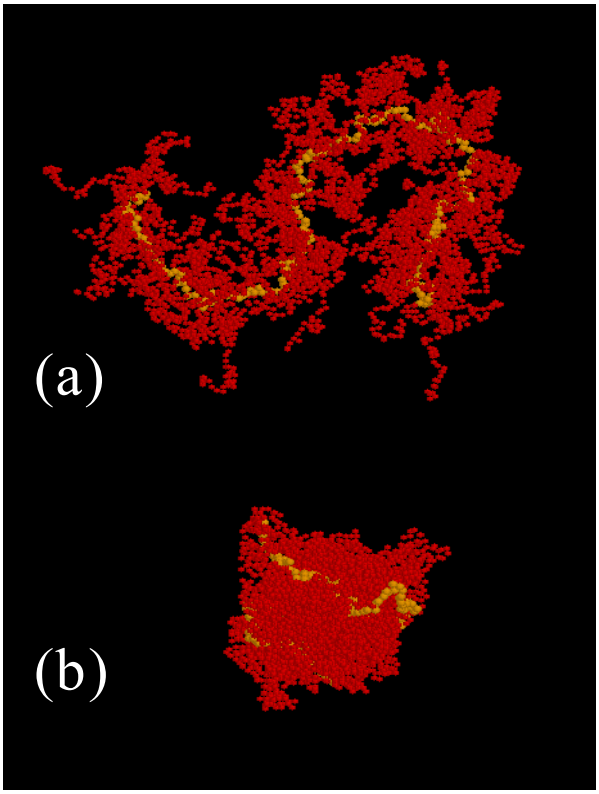

Figure 5.2 Snapshots from molecular dynamics simulations of (a) stretched, and (b) collapsed comb polymer. Color code: side-chain (red), backbone (yellow).

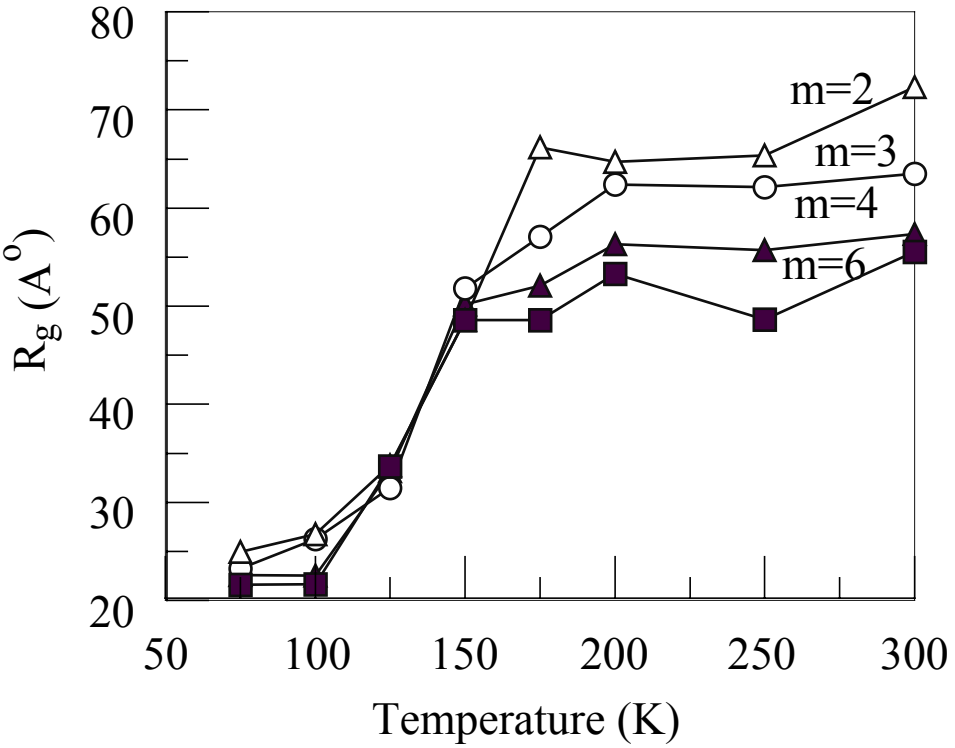

Figure 5.3 Radius of gyration of the whole molecule as a function of temperature for side chain grafting distances m=2, 3, 4 and 6.

The transition from a swollen state at high temperatures to a collapsed state at low temperatures is exhibited over a relatively narrow range of temperature, approximately 50K. Plotted in Fig. 5.4 is the probability distribution of the end-to-end distance of the backbone for an *m*=2 comb polymer at different temperatures. Each plot represents a time average of a single comb polymer molecule after equilibration. Double peaks are apparent in the probability distributions in the vicinity of the transition temperature. This is a clear indication that there are two preferred states at the transition, which is characteristic of a first-order transition. The conclusion of a first-order transition for a

structure of this type is consistent with results from recent bond-fluctuation model based Monte-Carlo simulations [9]. It is also consistent with the experimental results reported by Sheiko *et al* [10] of a rod-globule transition of poly (n-butyl acrylate) brush molecules adsorbed on a water layer. In this experiment, a discrete transition occurred upon lateral compression of the monolayer that was visualized using scanning force microscopy. They observed co-existence of rod and globule phases at the critical point, which indicates a first-order transition.

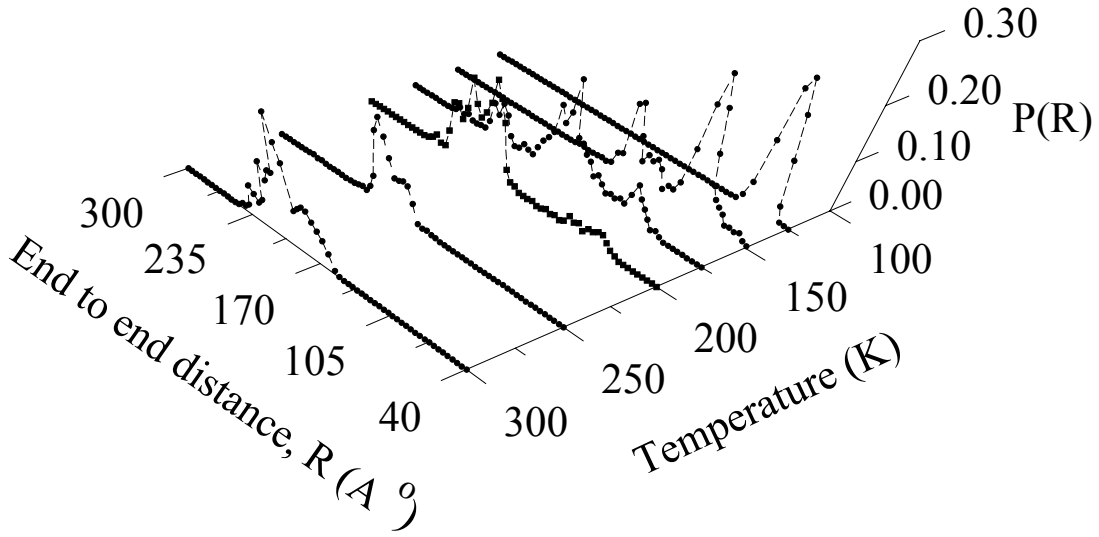

Figure 5.4 Probability distribution of the end-to-end distance R for isolated comb polymer with N=200, m=2 and n=40, at temperatures T=125, 150, 175, 200, 250 and 300 K.

To characterize the timescale of the collapse transition, simulations were carried out in which the temperature of brush molecules with different m values was quenched using a Nose' thermostat from an average temperature of 300K to 100K (i.e. from above to below

the transition temperature range). Plotted in Fig. 5.5 is the average radius of gyration R_g for the backbone as a function of time for molecules with different *m* values calculated from these simulations. Each plot represents average over five starting configurations. For reference, the temperature averaged over the simulations as a function of time is also plotted. In all the cases the molecules relax from their initial extended structures to the final globule structure in less than about 0.5 ns. This time value provides an estimate for the response time of a smart valve created from these structures.

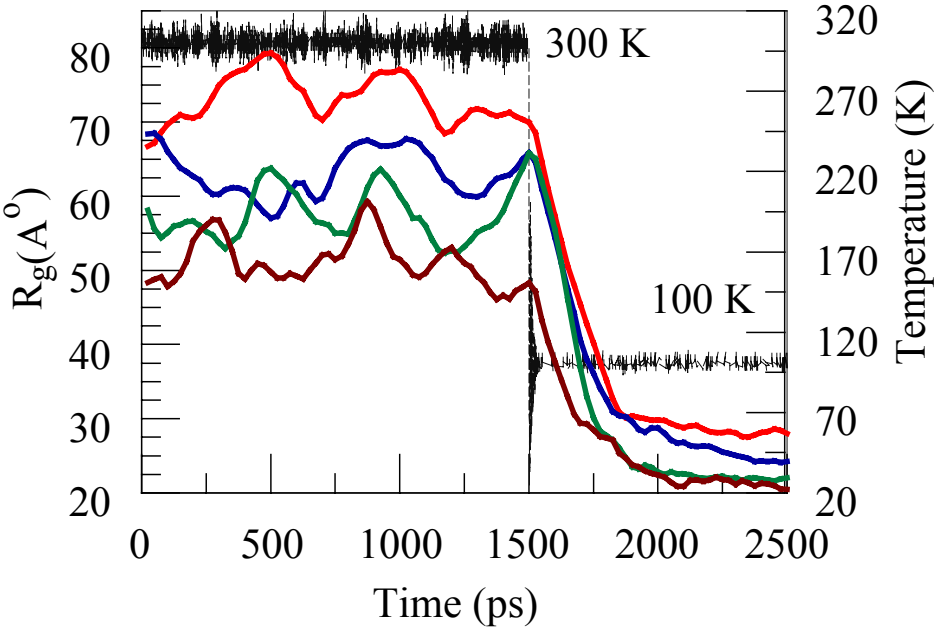

Figure 5.5 Plot of Rg vs. time for a comb polymer with N=200, n= 40 and m=2 (red), 3 (blue), 4 (green) and 6 (brown). The isolated molecules were quenched from a temperature T=300K to 100K. Temperature of the system as a function of time is shown in black for reference.

5.4 Brush Molecules inside the Slitpore as Smart Molecular Sieves

When attached to the interior walls of a slit pore comb polymers form a planar brush with individual molecules stretching away from the attachment points due to excluded volume interactions. The system modeled consists of comb polymer molecules (B) of N=100, m=4 and n=30, end-attached to two opposing walls. The in-plane x and y dimensions of the slit pore are 52σ x 54σ, respectively, and each wall is separated in the z direction by 74σ. The pore walls are modeled with frozen atoms placed on a (111) plane of a face centered cubic lattice with lattice constant $2^{1/2}\sigma$. The pore is grafted with nine brush molecules on a rectangular lattice with a grafting distance of 17.65σ between attachment points. The wall separation and grafting distances are about 2 times and one-half, respectively, of the end-to-end distance of a single comb molecule in its extended state, and about 8 and 2 times, respectively, of a comb molecule in its globule state. Purely repulsive nonbonded interactions using the parameters given above are used for the brush-wall and solvent-wall interactions. The brushes are immersed in monomeric solvent molecules (S) of the same size and mass as that of the beads of the comb molecules. Periodic boundary conditions are applied in the two directions parallel to the grafting surface. The total number of atoms in the system (excluding wall atoms) is N_t=96031 at a reduced number density of $N_t\sigma^3/V = 0.45$. The temperature of the system was chosen to be in the stretch-collapse transition region such that by proper choice of solvent-brush interaction pore opening and closing can be demonstrated. For a solvent with $\varepsilon_{BS}/\varepsilon_{BB} > 1$, the solvent-comb interaction is more attractive than the comb-comb interaction, thereby forming a good solvent for the combs. A solvent with $\varepsilon_{BS}/\varepsilon_{BB} < 1$ forms a poor solvent. For a solvent with $\varepsilon_{BS}/\varepsilon_{BB} = 1$, the B-B as well as B-S interactions

are equally preferred and the brush is said to be in the theta condition. The nanopore system was studied under different solvent qualities, with ε_{BS} ranging from 0.1 to 0.8 kJ/mol ($\varepsilon_{BS}/\varepsilon_{BB}$ between 0.2 and 1.6).

Plotted in Fig. 5.6 is the density of monomers belonging to comb molecules as a function of distance from the grafting surface at different solvent qualities. In a good solvent, the solvent molecules wet the grafted layer and the result is a stretched brush covering the entire volume across the pore. In a poor solvent, interaction among monomers of the comb polymers is preferred over interaction with solvent molecules and the comb polymer molecules collapse on the grafting surface, expelling the solvent molecules into the open space left in the pore. At the theta condition, the comb polymers adopt an intermediate structure, and the pore is partially open. It takes approximately $2x10^5$ simulation time steps to open a closed pore, which is about 0.5 ns.

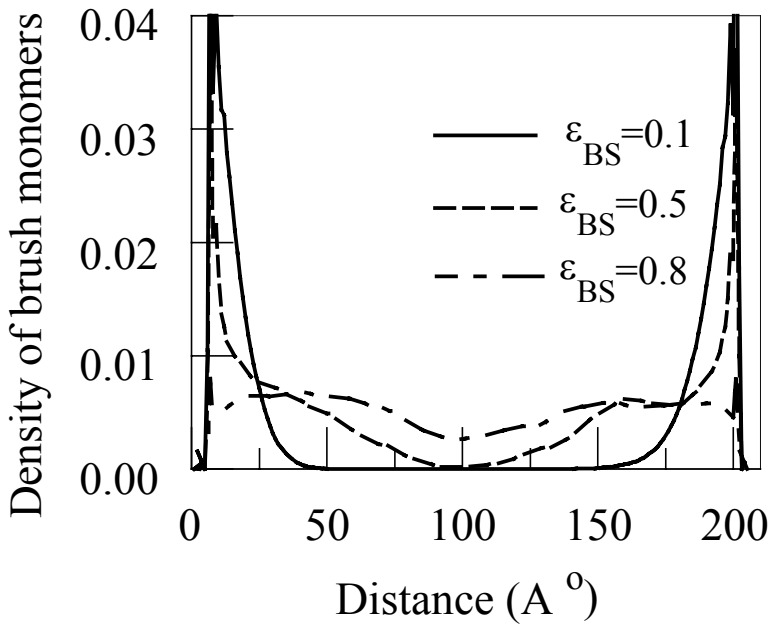

Figure 5.6 Density profiles of brush monomers across the pore at ε_{BS} = 0.1, 0.5 and 0.8 kJ/mol.

Snapshots of the system from the simulations in Fig. 5.7 depict the pore structure at the three different solvent conditions. Solvent molecules are not shown for better visualization of the brush. Plotted in Fig. 5.8 is side chain monomer density as a function of distance from the side-chain attachment point for a good solvent (ε_{BS} = 0.8 kJ/mol). This plot suggests that the side chains form an impermeable structure of radius 10σ around the main chain causing a significant overlap of adjacent brush molecules that are grafted at a distance 17σ.

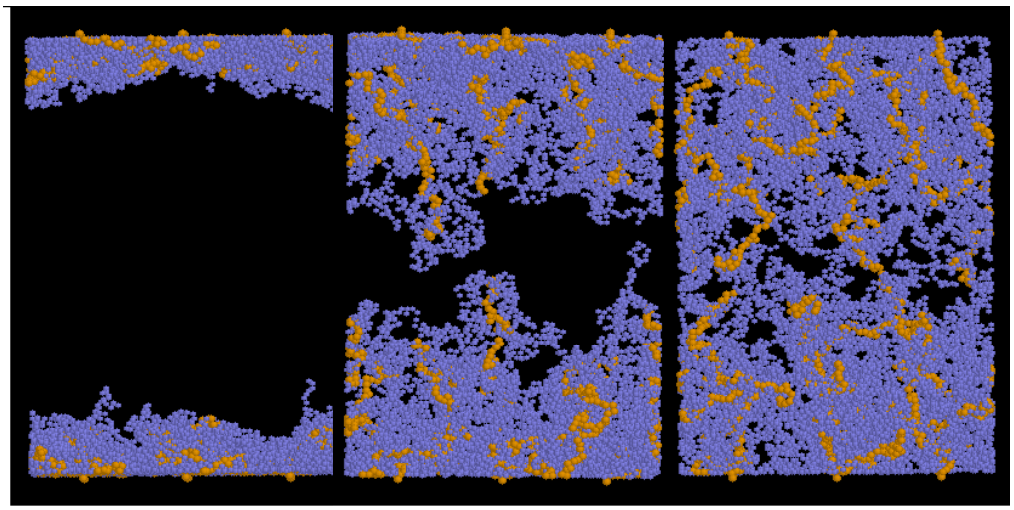

Figure 5.7 Snap shots from MD simulations of the nanoporous system for ε_{BS} =0.1 (left), 0.5 (center) and 0.8 (right) kJ/mol. Solvent molecules are not shown for better visualization of the brush structure. Color code: side chains (blue) and main chain (yellow).

It is apparent from the snapshots of the nanopore structure that comb polymer molecules grafted inside the pore could act as barriers for large molecule transport in the presence of a good solvent. To characterize the selectivity of the system for molecular separation, the transport of free oligomers of different lengths through the system under an external force was modeled. The oligomer chains interact purely repulsively with all other species in the system. A constant force F_e was applied in the x- direction of the pore channel on each bead belonging to the free chains. This artificial external force is analogous to an electric field acting on a charged polymer or a field due to chemical potential gradient in the x-direction. Ideally, collapsed comb molecules in a poor solvent would offer little resistance to the transport of oligomers and the dynamics would reduce to transport of a free chain in a monomeric solvent under an external force. Conversely, in a good solvent

the network of stretched brush molecules would trap a diffusing chain that is larger than the open space remaining in the pore. Plotted in Fig. 5.9 (bottom panel) is the center-of-mass displacement in the direction of the porechannel as a function of time for an oligomer chain containing 200 monomers drifting under an external field $F_e = 0.0162\varepsilon/\sigma$. For the open pore (corresponding to the solvent conditions for the system illustrated in the left frame of Fig. 5.7), the chain is able to move through the pore, while for the closed pore chain diffusion is not apparent. Plotted in Fig. 5.9 (top panel) is the mean square displacement of the oligomer center of mass from the simulation averaged over a large number of starting points. In the open pore averaged mean-square displacement of the chain varies with time as t^2, characteristic of a drift-like motion under an applied force. In the case of the closed pore the applied force attempts to push the molecule through the comb structure. As the process has to compete with the relaxation dynamics of the brush molecules, which is very slow, the polymer chain gets trapped in the brush network. The average size of the oligomer chain is $R_g \approx N_p^{3/5} a = 24\sigma$, which is larger than the distance between two grafted brush molecules. This implies that the polymer chain cannot migrate as a sphere through the structure, and has to translate by reptation, a much slower process compared to free translation [11].

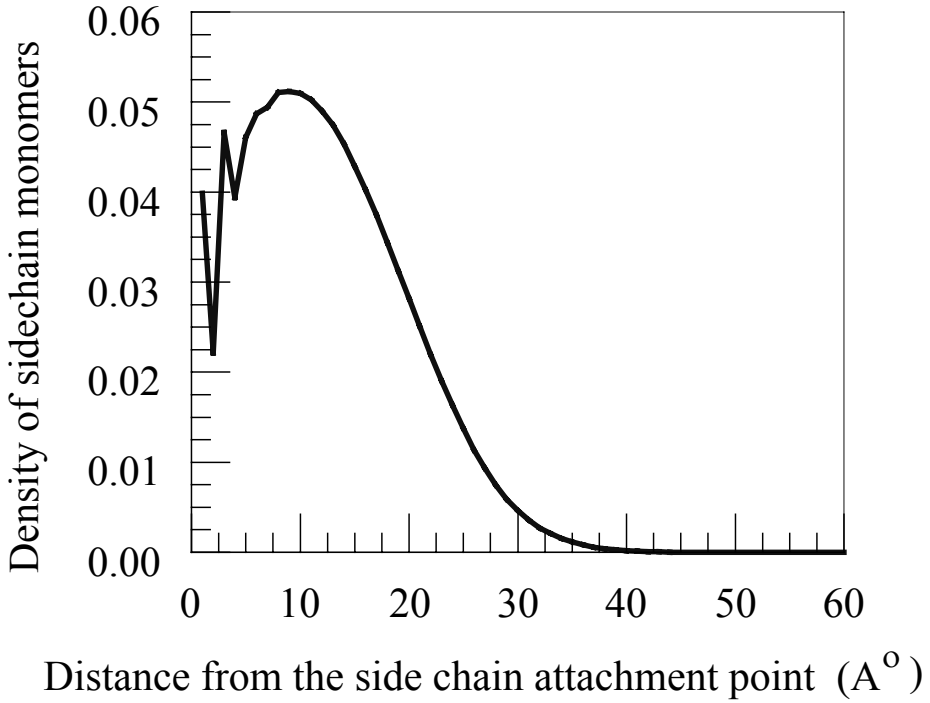

Figure 5.8 Density profile of side-chain monomers around the comb polymer. The number density of side-chain monomers is plotted as a function of xy- component (parallel to the grafting surface) of distance from the backbone under ε_{BS} =0.8 kJ/mol.

It is expected that a chain with a size smaller than the grafting distance *d* between the brush molecules can migrate easier than an oligomer larger than the grafting density. A molecule with $R_g < d$ could make its way through the region in between the grafted comb polymers which is less densely occupied by chains of the comb polymers. To test this expectation, simulations were used to characterize the transport behavior of oligomer chains of different sizes through the system containing a good solvent. The center-of-

mass displacement in the direction along the pore channel as a function of time is plotted in Fig. 5.10 for oligomer chains of size N_p = 20, 50, 100 and 200 under an external force $F_e = 0.0162\varepsilon/\sigma$ per monomer.

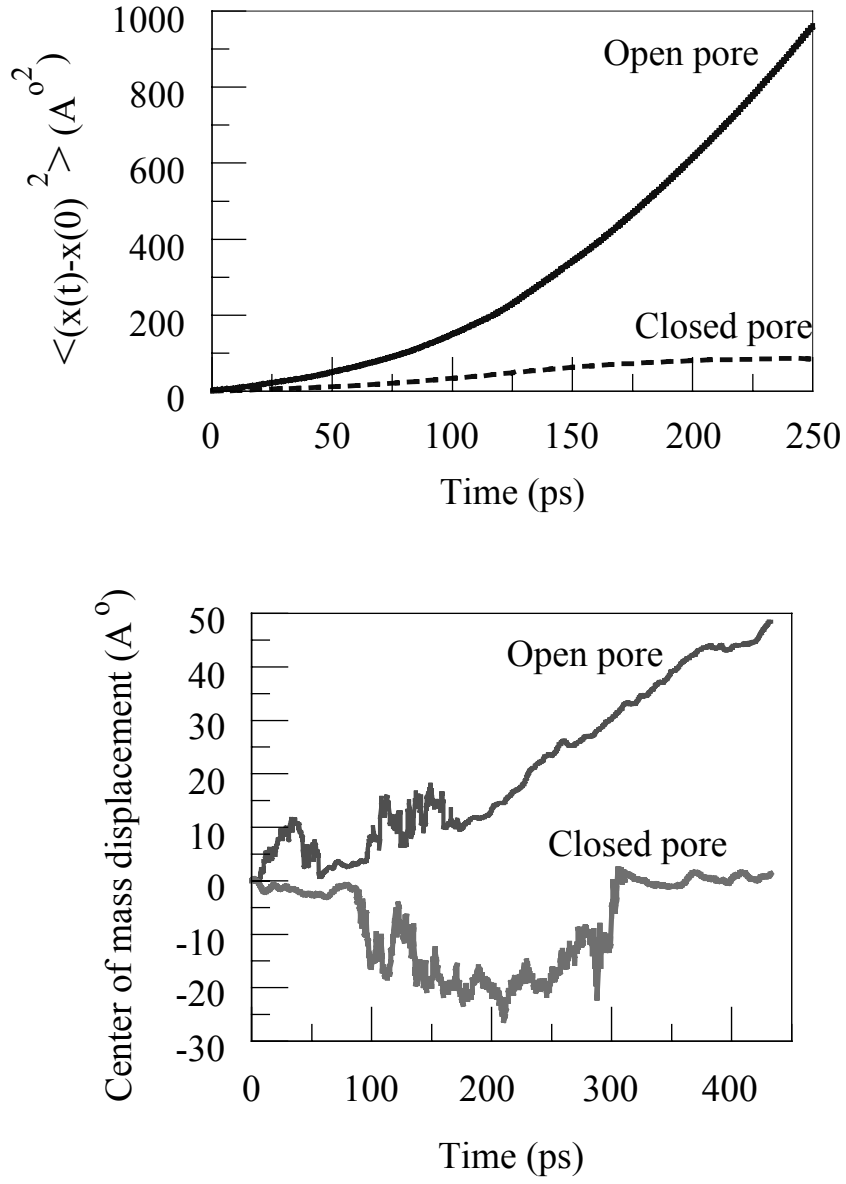

Figure 5.9 Mean square displacement of center of mass (Top) and center of mass displacement (Bottom) as a function of time for a free polymer chain of length N_p=200, under an external force F_e=0.0162ε/σ per monomer.

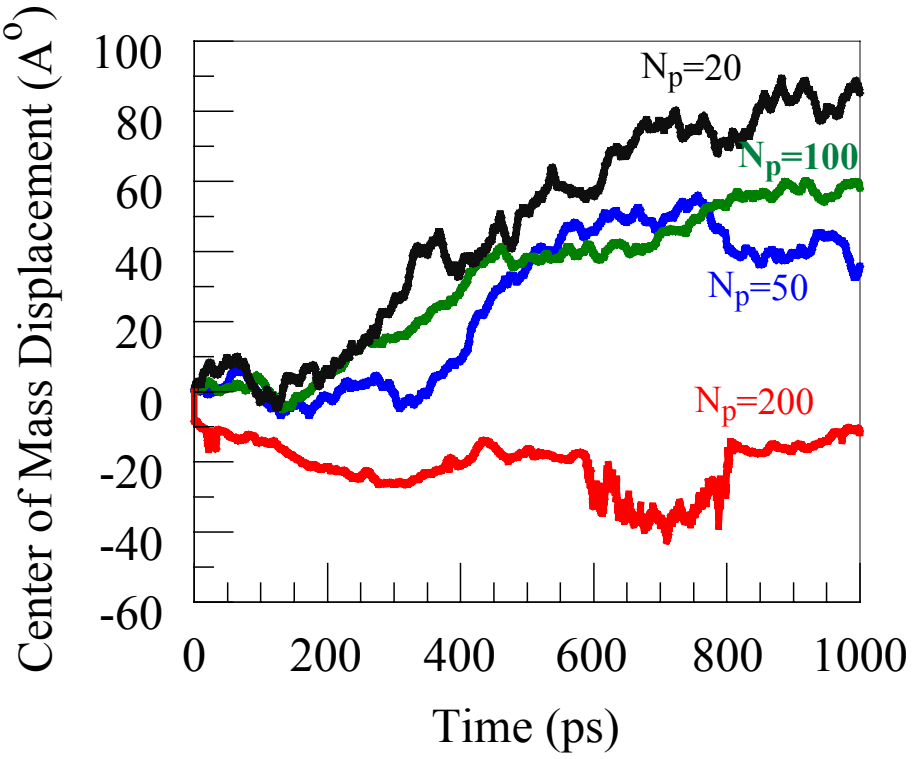

Figure 5.10 Center of mass displacement versus time for polymer chains of length N_p=20, 50, 100 and 200, through a closed pore. Fe=0.0162 ε/σ per monomer.

The N_p = 20 chain, which has an average size $R_g \approx 6.034\sigma$, translates through the system at a fairly steady velocity. For the N_p=50 and 100 oligmers, with $R_g \approx 10.45\sigma$ and 15.85σ respectively, the center-of-mass displacement plot shows a migration over a distance of about 50A° followed by a plateau. This distance of free translation of $\sim 18\sigma$ approximately corresponds to the grafting distance $d=17.65\sigma$, suggesting that the molecules are large enough to be hindered by the brush molecules as they diffuse. For N_p=200, the size $R_g \approx 24\sigma$ is larger than d, and the center-of-mass displacement does not indicate translation. However, as noted earlier, large molecules can reptate in the

direction of the field, which is a slower mechanism that is not observed in the time scale of our simulations. It may be noted that Fig. 5.10 shows a higher displacement for N_p=100 oligomer than for N_p=50 oligomer, which is out of the general trend. The reason for this discrepancy is that, in this set of simulations, N_p=50 oligomer finds itself trapped by a grafted brush molecule along its trajectory before N_p=100 oligomer does. Better statistics of trapping events are needed to further characterize the size dependency of oligomer diffusivity in the long time regime. This could be achieved through longer simulations or multiple simulations with different initial oligomer positions.

In general, the following observation can be made about the diffusion of chain molecules through the proposed nanoporous system under an external field. In the case of an open pore (under a poor solvent condition) chains can easily drift along the central region free of obstacles. The translocation is governed by a diffusion coefficient that varies as $D \sim 1/N_p$, as given by Rouse dynamics. In the case of a closed pore (good solvent), individual comb polymer molecules can be thought of as protrusions from the grafting surface with an average distance d between them. The orientation of these protrusions fluctuates about the normal to the grafting surface. There are two possibilities based on the size of the diffusing chain molecule. For molecules smaller than the passage between grafted comb polymers, Rouse dynamics still holds, with the combs acting as obstacles in their path. However, chains much larger than d feel topological constraints formed by the grafted combs and are forced to move by reptation. The reptation model predicts a diffusion coefficient that varies with chain length as $D \sim 1/N_p^2$. By a proper choice of d, N, n, and m a switchable molecular gate can be designed that screens molecules larger than a

certain critical size. It should be pointed out that surface grafted molecular architectures with precise parameters *d*, *N*, *n*, and *m* are experimentally realizable. For example, surfaces grafted with hyperbranched molecules with controllable parameters such as grafting density and degree of polymerization have been prepared [12, 13].

5.5 Conclusions

A stimuli-responsive nanoporous system whose functionality is based on a rod-globule transition in comb polymer molecules has been characterized using molecular dynamics simulations. The design consists of comb polymer molecules attached to the inside of a slit pore. The comb structures collapse in a poor solvent to open the pore and stretch in a good solvent to close the pore. Simulations of stretch-collapse transitions in isolated comb polymers indicate two-phase behavior characteristics of a first order transition, and that the transition can be completed in about 1 ns. Simulations of comb brushes attached to the inside surfaces of a slitpore immersed in a pool of explicit solvent molecules demonstrated the feasibility of opening and closing a pore in response to solvent quality. Simulations of oligomer chains in the pores also demonstrated that pore closing can be used to inhibit diffusion, and in a closed pore chains with sizes smaller than the passage between the grafted comb polymers can drifted relatively easily as compared to chains that are larger in size.

References

[1] Y. S. Park, I. Toshihiro, and Y. Imanishi, Macromolecules**, 31**, 2606 (1998).

[2] Y. S. Park, I. Toshihiro, and Y. Imanishi, Langmuir, **16**, 5376 (2000).

[3] M. Gerle, K. Fischer, S. Roos, A. H. E. Muller,, Manfred Schmidt, S S Sheiko, S. Prokhovora and M. Moller, Macromolecules, **32**, 2629 (1999)

[4] M. Wintermantel, M. Gerle, K. Fischer, M. Schmidt, I. Wataoka, H. Urakawa, K. Kajiwara, and Y. Tsukahara , Macromolecules **29**, 978 (1996).

[5] S. S. Sheiko, M. Moller, Dendimers II, Topics in Current Chemistry **212**, 137 (2001).

[6] DL_POLY is a package of molecular simulation routine written by W. Smith and T. R. Forester, copyright The Council for the Central Laboratory of the Research Councils, Daresbury Laboratory at Daresbury, Nr. Warrington (1996). For details see http://www.dl.ac.uk/TCSC/Software/DL_POLY/main.html

[7] K. Binder, ed., Monte Carlo and Molecular Dynamics Simulations in Polymer Science, Oxford University Press; Oxford (1995).

[8] Y. Rouault, and O. V. Borisov, **29**, 2605, (1996).

[9] V.V. Vasilevskaya, A.A. Klochkov, P. G. Kkalatur, A. R. Khokhlov, and G. ten Brinke, Macromolecular Theory and Simulations, **10**, 389 (2001).

[10] S. S. Sheiko, S. A. Prokhorova, K. L. Beers, K. Matyjaszewski, I. Potemkin, A. R. Khokhlov, and M. Moller, Macromolecules **34**, 8354 (2001).

[11] M. Doi, S. F. Edwards, The theory of polymer dynamics, Oxford University Press; Oxford (1988).

[12] Y. Zhou, M. L. Bruening, D. E. Bergbreiter, R. M. Crooks, and M. Wells, J. Am. Chem. Soc., **118**, 3773 (1996).

[13] H. Mori, A. Bo1ker, G. Krausch, and A. H. E. Muller, Macromolecules, **34**, 6871 (2001).

6 Structure of Neurofilaments

6.1 Introduction

The interest in studying neurofilaments arises because they have a structure that resembles a cylindrical polymer brush that has side chains emanating from a rigid backbone [1]. The side chains of a neurofilament are unstructured polypeptides. The neurofilaments form an assembly inside the axon in which individual filaments run parallel to the axon length. It is well established in the neuroscience literature that this remarkable architecture, while allowing for nutrients and ions to pass through, provides mechanical support to the axon. However, the precise mechanism that imparts neurofilaments this functionality is not yet established. It is important to investigate the structure and function of neurofilaments since a defect in their structure/assembly is thought to be a molecular link to several neurodegenerative disorders [2]. A better understanding at a molecular level of how these structures function and under what circumstances they lose their functionality could shed light on a piece of the puzzle of several neuromuscular disorders. Recent investigations have proposed a polymer brush structure for the neurofilament to explain their function [3, 4]. Can the techniques described in the previous Chapters be utilized to investigate this further? Before stating the objectives of this Chapter a brief background on neurofilaments from a biological point of view is presented.

6.2 Background

Neurons communicate with cells by means of cytoplasmic extensions (*processes*) called axons that reach out to their synaptic targets. Subsequent to their formation and reaching the target cells axons undergo a radial growth, a process associated with a local accumulation of neurofilaments within the expanding region. Neurofilaments are intermediate filaments (IFs) that are intermediate in size between actin filaments and microtubules [1]. They are cylindrical structures having polypeptide sidearms extending 40-50 nm from 10 nm diameter cores (Fig. 6.1). They are assembled from three major polypeptides, NF-L, NF-M and NF-H, with different molecular masses (L, M and H specify low, medium and high relative molecular mass, respectively) that are formed in neuroblasts. Each of the polypeptides shares a homology over a 300 amino acid sequence that forms the neurofilament core. The remaining polypeptide sequences in NF-M and NF-H extend beyond the core region to form sidearms.

Neurofilaments along with other proteins after their synthesis in the cell body (perikaryon) move down the axon at an average rate of about 1mm per day in a series of jumps [1, 5, 6]. This movement, which is essential for the growth and survival of axons, is referred to as “axonal transport”. The precise mechanism of axonal transport is unknown. There is a debate about whether the neurofilaments and microtubules are delivered as subunits and then assembled or if their assembly is necessary before they can be transported [7]. There is an additional uncertainty regarding how they are transported that has led to the proposal of two models [8]. In the first model, neurofilaments bind to motor proteins such as dyein/kinesin and these motors move along the stationary

microtubules to transport the neurofilaments along the axon. In the second model, neurofilaments bind directly to microtubules and the microtubules are moved along the axon by motor proteins.

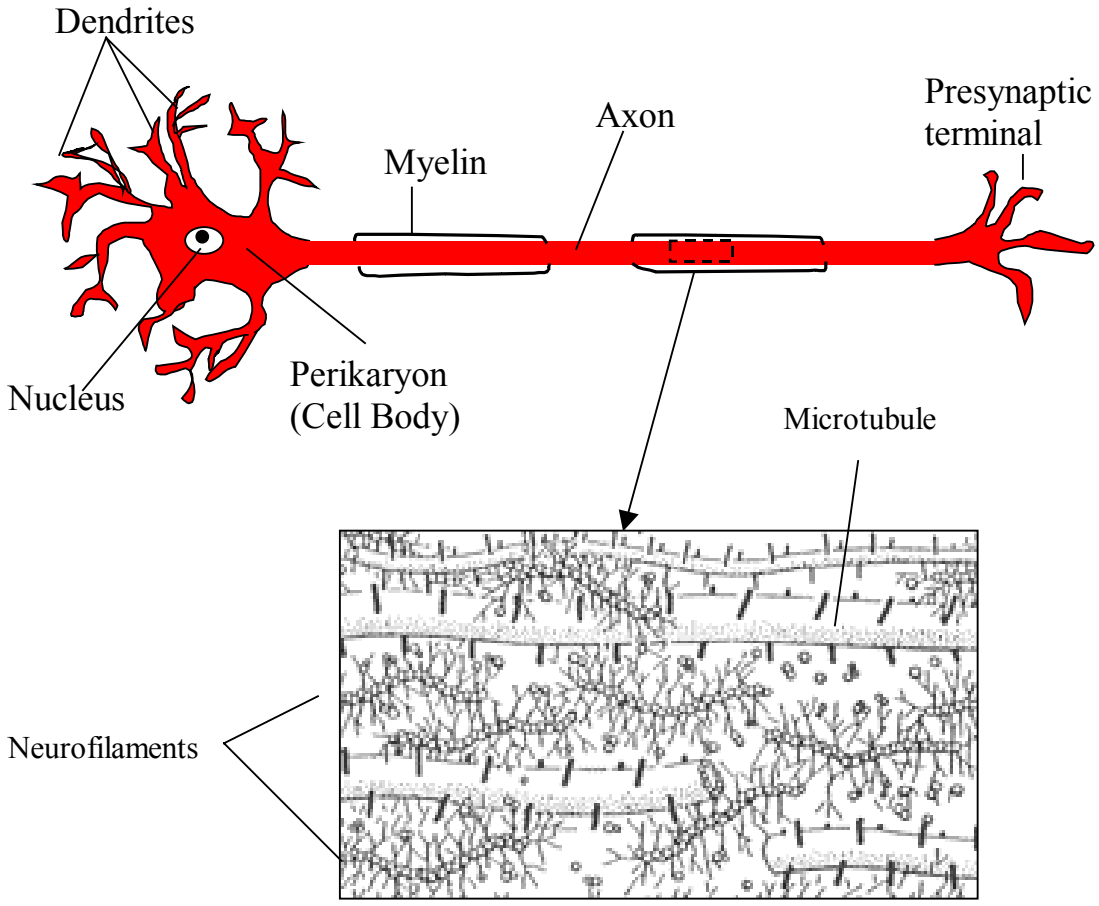

Figure 6.1 Illustration of a neuron (Top) and neurofilaments along with other cytoskeletal elements (Bottom).

Despite the ongoing debate about the molecular mechanism of transport it is fairly well established that regional accumulation of neurofilaments, a process that brings about radial growth of axons, is brought about through a slowing down of axonal transport. Evidence has been provided that the slowing down of neurofilament transport down the

axon is regulated by phosphorylation of site-specific LYS-SER-PRO (KSP) motifs that are present in the C-terminal domains of NFH and NFH (that form neurofilament side arms) [6, 7, 9]. In other words, phosphorylation (a process catalyzed by enzymes called *kinases* that results in transfer of phosphate from ATP to target proteins) causes radial growth of axons through local neurofilament accumulation. Besides increasing neurofilament number, studies suggest that phosphorylation increases the interfilament spacing as well [10]. Presumably, phosphorylation causes a change in the structure of neurofilaments that slows down or stops their movement. While phosphorylation regulated neurofilament transport and accumulation is critical for healthy functioning of neurons, a disruption in neurofilament transport due to physical or chemical injuries can cause neurodegenerative diseases [2]. For example, accumulation of excess neurofilaments in the axons is associated with several neuromuscular diseases, in particular amyotrophic lateral sclerosis (ALS - Lou Gehrig's disease). Experiments on transgenic animals with neurofilament overexpression or mutations that disrupts normal filament stiochiometry or assembly have also produced abnormal neurofilament accumulation similar to that observed in ALS [3]. Therefore, there is clear link between abnormal neurofilament accumulation and the neurodegenerative disease process. Additionally, the biological structure/function of neurofilament assembly is likely to depend on the interaction between neurofilaments that is thought to be regulated by the extent of phosporylation of the side arms. From this point of view, an understanding of the structure and the mechanism that determines the interfilament spacing of neurofilaments is very critical.

Equally importantly, an understanding of neurofilament structure is essential in studying the response of axons to mechanical injuries. One of the main features of traumatic brain injuries is axonal damage that involves disruption of its cytoskeletal assembly [11]. It has been observed that in addition to the magnitude of force applied the rate of strain during the trauma affect the extent/nature of injury. Presumably, this depends on how fast the viscoelastic polymer network (cytoplasm consisting mainly of neurofilaments) responds to the applied force. A detailed study of the structure of neurofilaments and the effect of phosphorylation may be useful in determining the critical strain rate beyond which the axon sustains permanent damage.

Three different models have been proposed for the mechanism(s) by which neurofilaments maintain the axon diameter. In the first, the sidearms are thought to be crosslinked between different neurofilaments; this lends mechanical stability to the structure [12, 13]. The second model suggests that Coulombic interaction due to a net negative charge of phosphorylated residues along the side arms result in long-range interfilament repulsion [14]. The third theory, recently proposed by Hoh and coworkers [3, 4], suggests that the side arms repel one another through entropic forces resulting from Brownian motion of the side chains. The Coulombic interaction due to phosphrylation is thought to affect only intra molecular interaction. An increase in the extent of phosphorylation expands the side arm and thereby increasing the interfilament distance. Evidence for this comes from two atomic-force microscopy (AFM) experiments [3]. In the first, images were obtained that clearly show an excluded region of material co-isolated with the filaments around individual neurofilaments on a mica

surface. Similar experiments with single NF-L polypeptides do not show an exclusion zone, suggesting that the assembled structure with free sidearms is needed to maintain the interfilament distance. The second piece of evidence for this model comes from distance-force curves for an AFM tip over neurofilaments that indicate the onset of repulsive forces at a distance starting about 50nm above the filament core. This is the height at which the sidearms are predicted to extend due to Brownian motion.

Presented in this Chapter are the results from molecular dynamics (MD) carried out to investigate the effect of phosphorylation on the size and structure of human NFH side arm. The results from MD are used in polymer brush models to determine the thickness of the filament. Finally, the results will be compared with experiments.

6.3 Primary Structure of Human NFH

The human NFH has been sequenced by Lees and coworkers [15]. The sequence of human NFH can be divided into three regions – an N-terminal domain of ~ 100 amino acids, a central helical domain of ~ 310 amino acids and a C-terminal domain of ~ 606 amino acids. The first two domains along with the N-terminal and helical domains of NFL and NFM form the filament core. The one letter amino acid sequence of the C-terminal domain of human NFH is given in Fig. 6.2.

One of the main features of the C-terminal domain that forms the side arm is that it is a polyampholyte, containing 24.1 % GLU (- 1 charged) and 25.7% LYS (+1 charged). In

FGPIPFSLPEGLPKIPSVSTHIKVKSEEKIKVVEKSEKETVIVEEQTEETQVTEEVTEE
EEKEAKEEEGKEEEGGEEEEAEGGEEETKSPPAEEAASPEKEAKSPVKEEAKSPAE
AKSPEKEEAKSPAEVKSPEKAKSPAKEEAKSPPEAKSPEKEEAKSPAEVKSPEKAK
SPAKEEAKSPAEAKSPEKAKSPVKEEAKSPAEAKSPVKEEAKSPAEVKSPEKAKSP
TKEEAKSPEKAKSPEKEEAKSPEKAKSPVKAEAKSPEKAKSPVKAEAKSPEKAKS
PVKEEAKSPEKAKSPVKEEAKSPEKAKSPVKEEAKTPEKAKSPVKEEAKSPEKAK
SPEKAKTLDVKSPEAKTPAKEEARSPADKFPEKAKSPVKEEVKSPEKAKSPLKAD
AKAPEKEIPKKEEVKSPVKEEEKPQEVKVKEPPKKAEEEKAPATPKTEEKKDSKK
EEAPKKEAPKPKVEEKKEPAVEKPKESKVEAKKEEAEDKKKVPTPEKEAPAKVE
VKEDAKPKEKTEVAKKEPDDAKAKEPSKPAEKKEAAPEKKDTKEEKAKKPEEKP
KTEAKAKEDDKTLSKEPSKPKAEKAEKSSSTDQKDSKPPEKATEDKAAKGK

Figure 6.2 Amino acid sequence of C-terminal domain of human NFH protein.

addition to this there are 53 serine residues that can attain a –2 charged state when phosphorylated. A fully phosphrylated C-terminal domain of NFH can have a net charge of –113. Another striking feature is that the segment includes 43 LYS-SER-PRO (KSP) motifs with either 3 or 5 residue spacers between them. The KSP repeats present in the sequence can be divided into two groups based on the presence or absence of K in the second amino acid position following the motif i.e. KSPXK or KSPXX (X is any residue

other than LYS). The serine residue in the KSP motif is identified as the phosphorylation site that explains the high degree of phosphorylation of NFH. The domain is also rich in PRO (~12%) that is fairly uniformly distributed along the domain suggesting an absence of a secondary structure. Secondary structure predictors have predicted a 20 % alpha-helix, and > 70% random coil structure for human NFH side arm. Circular dichroism (CD) measurements have confirmed that the side arm contains about 20 % alpha-helix structure. Recent AFM experiments by Aranda-Espinoza [16] *et al.* have indicated that NFH side arms have a multiple domain structure. The presence of multiple (~4) domains was attributed to loops along the neurofilament that result from salt bridges between oppositely charged residues.

6.4 Effect of Phosphorylation on NFH side arm size: Results of Molecular Dynamics Simulations

Molecular dynamics (MD) simulations were carried out to investigate the effect of phosphorylation on C-terminal domain of NFH. The all-atom parameterization of the AMBER force field ff99 was used in the simulations. The initial model of the chain was built using the LEAP module of AMBER version 7 [17]. All residues except for the phosphorylated serine, phosphoserine (SEP) are included in the Amber library. The forcefield parameters for the SEP residue were obtained using the generalized Amber force field (GAFF) included in the Antechamber module of AMBER. The partial charges on the atoms of the SEP residue were derived by following the procedure described in AMBER documentation [17, 18, 19]. Gaussian was used to calculate the obtained electrostatic potential (ESP) at the molecular surfaces at the HF level of theory using the

6-31G* basis set. Atom centered charges were obtained using the restrained electrostatic potential (RESP) fitting module of AMBER [17, 19]. The basic idea behind the electrostatic potential charge fit is that a least squares fitting algorithm is used to derive a set of atom-centered point charges that best reproduce the electrostatic potential of the molecule.

Four different chains NFH_0, NFH_{25}, NFH_{50}, and NFH_{100} corresponding to the phosphorylation content 0, 25, 50 and 100% respectively were studied. While NFH_{100} included all phosphorylated serine residues, every second and every fourth serine residues along the sequence were phosphorylated for NFH_{25} and NFH_{50}, respectively. The completely extended initial model of the chain was energy-minimized for 2000 steps to remove any unfavorable contacts between atoms.

The MD simulations were carried out using an implicit solvent description; i. e. the solute (NFH) was modeled with out explicit water molecules but the calculations considered the effects of a high-dielectric solvent that is approximated by a continuum electrostatic model. This was implemented using the GB/SA option included in AMBER version 7, generalized Born (GB) solvent and solvent accessible surface area (SA) – that considers the effect of solute exposed to the solvent [20]. The use of an implicit solvent reduces the computational time by orders of magnitude as it eliminates several thousands of water molecules that also enhances the rate at which the solute explores the configurational space (absence of viscous drag). The systems were equilibrated at a temperature of 300K for about 50 ps. This was followed by a MD simulation of 9 ns. Sampling was begun

after the polypeptide chains attained their average size and began to fluctuate around a mean value. The time evolution of potential energy and the radius of gyration of the polypeptide chain during a MD simulation are plotted in Fig. 6.3 for NFH_0. A typical run of 9 ns took about 60 days of CPU time on a windows cluster using 8 processors (2 GHz).

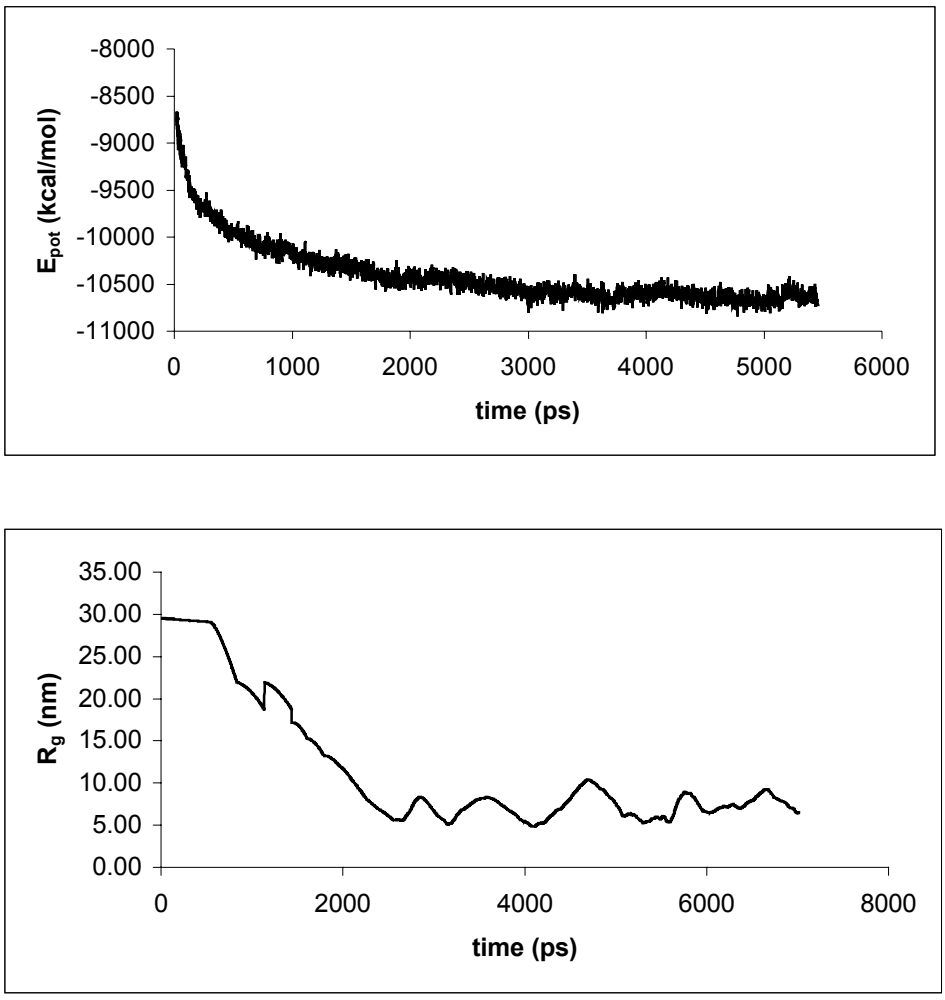

Figure 6.3 Time evolution of potential energy (Top) and radius of gyration (Bottom) of NFH_0 during a MD simulation.

Illustrated in Fig. 6.4 are snapshots from MD simulations for NFH_0 and NFH_{100} with the polypeptide backbone represented using a ribbon model. The phosphorylated serine

residues are represented by a ball-stick model for reference. The polypeptide chains have several turns but the helical content is <18%. The presence of PRO with a near uniform distribution along the sequence explains the absence of predominant helical regions.

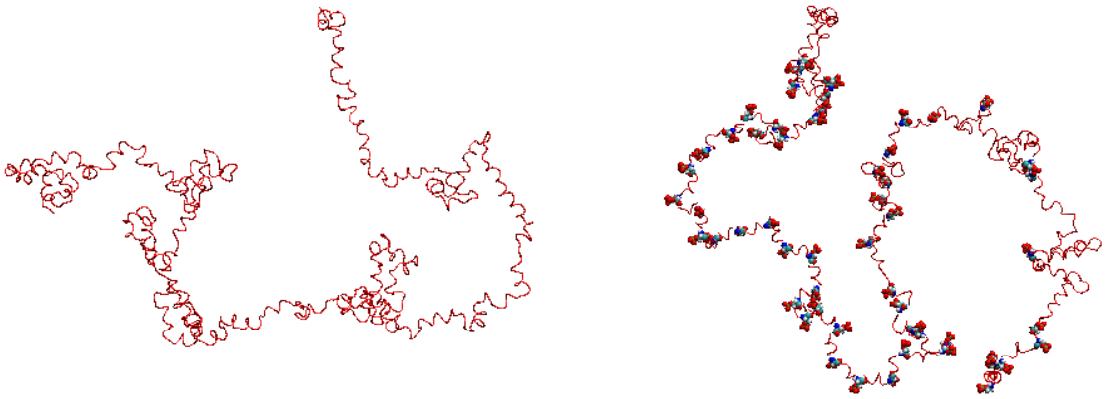

Figure 6.4 Snapshots from MD simulations for NFH_0 (Left) and NFH_{100} (Right). SEP residues are represented by a ball-stick model.

The configurations show distinct loop like formations along the chain that occur with a higher probability in NFH_0 as compared to NFH_{100}. To investigate this further, MD trajectories were followed to observe the loops in the chains. These loops are transient and they from and break during the chain's motion. A careful analysis of the sequence and the MD simulations indicated that these loops are formed as a result of electrostatic bridges formed between oppositely charged residues along the chain. When dephosphorylated, the side arm is essentially neutral (net charge = -1). However, on average, every other residue is charged (~24 % GLU and ~25% LYS). Therefore, electrostatic bridges between positively charged LYS and negatively charged GLU could lead to energetically favorable loops. In these loops several residues orientate themselves to maximize the interaction between LYS-GLU pairs.

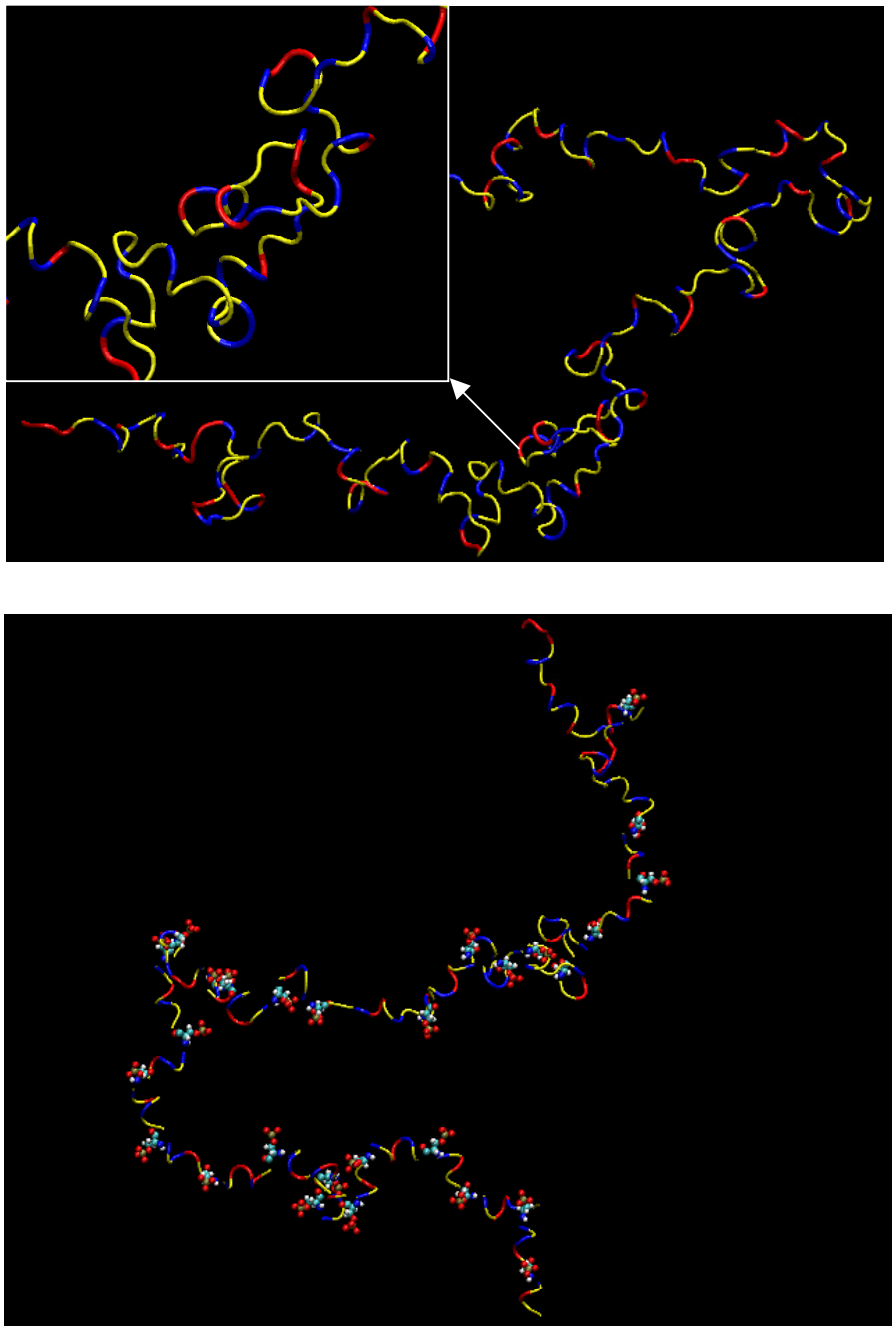

Figure 6.5 Top: A segment between residues 180-430 of the NFH_0 chain showing loops. One of the loops is zoomed in to show LYS and GLU contacts. Bottom: The same part of the chain for NFH_{100}. Color Code: LYS (Blue), GLU (Red). SEP is represented by a ball-stick model.

These loops illustrated in Fig. 6.5 are absent in the initial 80-residue segment that is highly negatively charged and is depleted with PRO. A preliminary investigation suggests that loop formation is facilitated by the local presence of oppositely charged LYS and GLU residues and the turn inducing PRO residue. Why then are the loops not formed to the same extent in the case of a completely phosphorylated NFH side arm? In the case of a completely phosphorylated sidearm, the presence of SEP, which has a charge –2 makes the loops unstable. Let us consider the chain segment between residues 85 and 410, which has 43 KSP motifs with either 3 or 5 residue spacers between them. Formation of a loop in this region brings several SEP residues in close contact, which from an electrostatic perspective is not favorable. This is exactly what the simulation results indicate. The NFH_{100} chain has no loops or only short loops in the KSP rich segment (between residues 85-410) and loops seem to be forming easily outside this region. The simulations indicated a decrease in the average number of loops as the extent of phosphorylation increased.

This breaking of local electrostatic bridges due to the electrostatic repulsion between phosphorylated serine residues directly affects the size of a NFH sidearm. Plotted in Fig. 6.6 is the radius of gyration (R_g) of a NFH sidearm as a function of the extent of phosphorylation. There is an increase in R_g of about 87 % from 0 to 100 % phosphorylated state. Aranda-Espinoza and co-workers have reported AFM experiments on neurofilament sidearms that indicated the presence of similar loops. However, they

suggested that salt bridges between SEP and LYS stabilized these loops. In the present work, the simulations do not provide evidence for salt bridges between SEP and LYS.

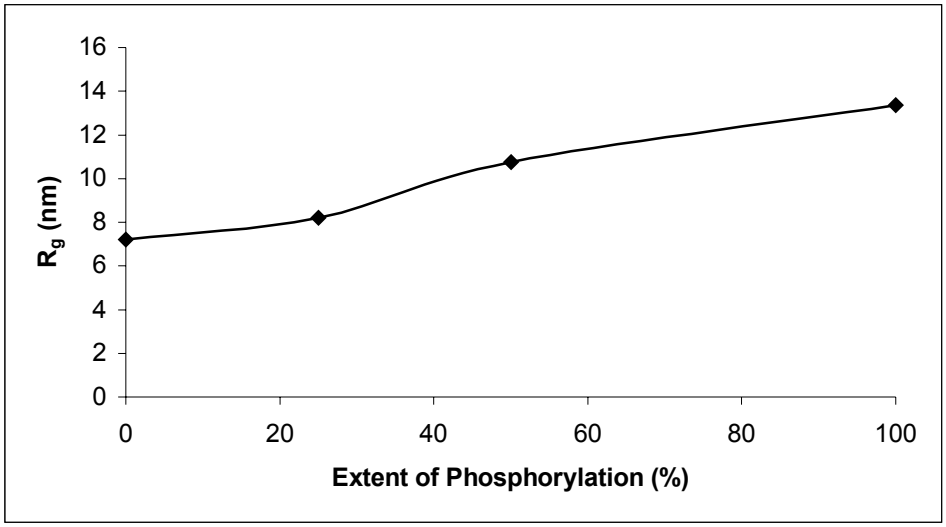

Figure 6.6 R_g as a function of % of phosphorylated serine residues.

Having determined the effect of phosphorylation on the size of a NFH side arm a polymer brush analysis based on excluded volume arguments is carried out to determine the extension of sidearms around the neurofilament core. The sidearms are considered as polymer chains grafted to a convex cylindrical surface. The radius of the cylinder is taken as the radius of the filament core R_c = 5 nm and a spacing of l = 3 nm between the sidearms was used [3]. The extension h of the sidearms from the filament core was calculated for the values of the extent of phosphorylation = 0, 25, 50 and 100 %. Plotted in Fig. 6.7 is the radius $R_c + h$ of the filament as a function of phosphorylation that varies between 25 to 45 nm for the dephosphorylated and completely phosphorylated states. The values of neurofilament radius predicted by our calculations are slightly lower than the

experimental values of 40- 80 nm reported in the literature. However, the results qualitatively agree with the experimental observations that indicate an increase in interfilament spacing caused by phosphorylation. The results can also explain the slowing down of neurofilament transport due to a phosphorylation-induced increase in the neurofilament size.

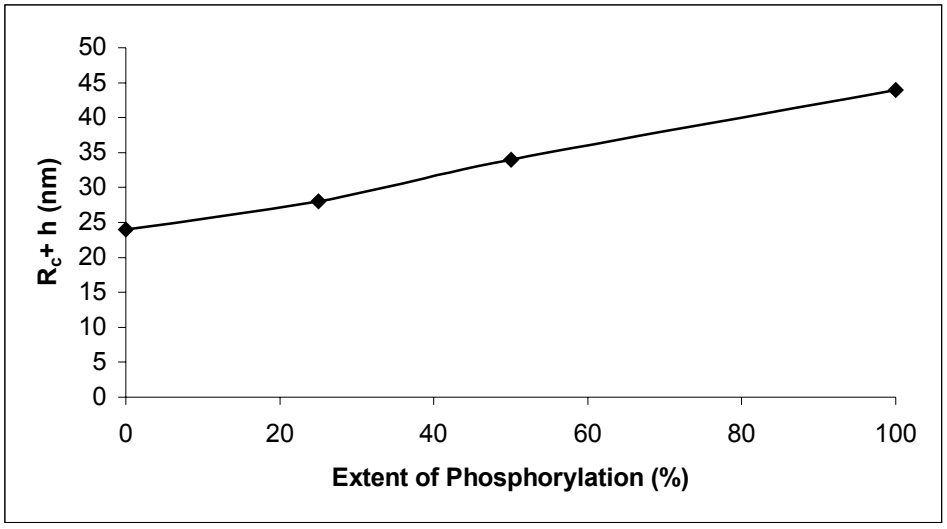

Figure 6.7 Neurofilament radius as a function of % of phosphorylated serine residues.

6.5 Conclusions

In conclusion, MD simulations were performed to characterize the structure of the C-terminal domain of the human NFH as a function of the extent of phosphorylation. These simulations indicated that phosphorylation significantly increases the side arm size, which in turn increases the neurofilament radius. The results showed that the dephosphorylated side arm is characterized by the presence of transient loops stabilized by electrostatic bridges between LYS and GLU residues. The breaking of these bridges

upon phosporylation seems to be the mechanism that increases the chain size. The results may be useful in understanding the molecular processes that lead up to several neuromuscular diseases.

References

[1] See for example `Neurofilaments', C.A. Marotta, Ed. (University of Minnesota Press, Minneapolis, 1983)

[2] J. H. Morrison, and P. R. Hof, Science, **278**, 412 (1997).

[3] H.G. Brown and J.H. Hoh, Biochemistry **36**, 15035 (1997).

[4] J.H. Hoh, Proteins: Structure, Function and Genetics **32**, 223 (1998).

[5] L. Wang, C.-L. Ho, D. Sun, R.K.H. Liem and A. Brown, Nature Cell Biol. **2**, 137 (2000).

[6] A. Brown, Nature, **1**, 153 (2000).

[7] P. W. Baas, and A. Brown, Trends in Cell Biology, **7**, 380 (1997).

[8] S. T. Brady, Nature Cell Biology, **2**, E43 (2000).

[9] C. Jung, and T. B. Shea, Cell Motility and the Cytoskeleton, **42**, 230 (1999).

[10] I. Sanchez *et al*. J. Cell Bio., **151**, 1013 (2000).

[11] D. H. Smith, and D. F. Meaney, Progress in Clinical Neuroscience, 6, 483 (2000).

[12] See for example J.F. Leterrier and J. Eyer, Biochem. J. **245**, 93 (1987)

[13] J.F. Leterrier, J. Kas, J. Hartwig, R. Vegners, and P.A. Jamney, J. Bio. Chem. **271**, 15687 (1996).

[14] M.J. Cardin, J.Q. Trojanowski, W.W. Schlaepfer and V.M. Lee, J. Neurosience **7**, 3489 (1987).

[15] J.F. Lees, P.S. Shneidman, S.F. Skuntz, M.J. Cardin, and R.A. Lazzarini, The EMBO Journal **7**, 1947 (1988).

[16] H. Aranda-Espinoza *et al.* FEBS Letters, **531**, 397 (2002).

[17] D.A. Case, D.A. Pearlman, J.W. Caldwell, T.E. Cheatham III, J. Wang, W.S. Ross, C.L. Simmerling, T.A. Darden, K.M. Merz, R.V. Stanton, A.L. Cheng, J.J. Vincent, M. Crowley, V. Tsui, H. Gohlke, R.J. Radmer, Y. Duan, J. Pitera, I. Massova, G.L. Seibel, U.C. Singh, P.K. Weiner and P.A. Kollman (2002), AMBER 7, University of California, San Francisco.

D.A. Pearlman, D.A. Case, J.W. Caldwell, W.S. Ross, T.E. Cheatham, III, S. DeBolt, D. Ferguson, G. Seibel, and P. Kollman. AMBER, a package of computer programs for applying molecular mechanics, normal mode analysis, molecular dynamics and free energy calculations to simulate the structural and energetic properties of molecules. Comp. Phys. Commun. **91,** 1 (1995).

[18] C. I. Bayly *et al*. J. Phys. Chem. **97**, 10269 (1993).

[19] P. Cieplak *et al*. J. Comp. Chem, **16**, 1357 (1995).

[20] V. Tsui, and D. A Case, Biopolymers, **56**, 275 (2001).